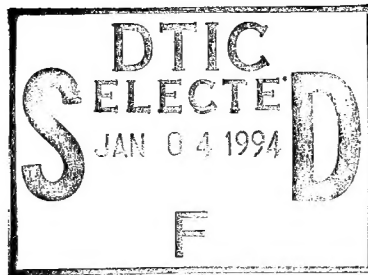


**CRREL REPORT**

**94-12**



# **Subsurface Radar Investigations at the Pegasus Glacial-Ice Runway and Williams Field, McMurdo Station, Antarctica**

Steven A. Arcone, Allan J. Delaney and  
Wayne Tobiasson

November 1994

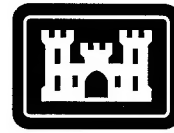


### ***Abstract***

Subsurface radar was used to profile ice and snow conditions on the Ross Ice Shelf at McMurdo Station, Antarctica, during mid-January 1993. Deconvolution and migration were often used to improve vertical resolution and spatial imaging. Profiles at a pulse center frequency of 400 MHz along the 3.2-km-long Pegasus ice runway show many low-density horizons above 9 m depth that are up to 30 m long. They are associated with air bubbles included during refreezing of meltwater and are interpreted as layers between a few and tens of centimeters thick. There is a strong reflecting horizon at about 9 m depth that is probably from brine intrusion as it is continuous with the intrusion into the snow to the east. Diffraction asymptotes give a dielectric constant near 3.2 for material above the brine level, a value that implies near-solid ice. Profiles at 100 MHz along the road between Pegasus runway and Williams Field in the accumulation zone show snow features such as layer deformation and intrusive brine layers that both abruptly and gradually change in depth. A single profile at a relic solid waste dump at Williams Field detected buried debris and ice within the upper 7 m. A survey of a suspected fuel spill shows some local disturbances near the center, but no excavation was done to verify the findings. Profiles traversing the sewage sumps at Williams Field outline the extent of the sewage deposition, and give depths to contaminated snow that closely agree with observation. Despite variability in dielectric properties, single-layer migration effectively improves the resolution of subsurface conditions. Recommendations are made for future surveys.

*Cover: Radar profiling at 400 MHz pulse center frequency along the Pegasus runway, January 1993.*

For conversion of SI metric units to U.S./British customary units of measurement consult ASTM Standard E380-89a, *Standard Practice for Use of the International System of Units*, published by the American Society for Testing and Materials, 1916 Race St., Philadelphia, Pa. 19103.



**US Army Corps  
of Engineers**

Cold Regions Research &  
Engineering Laboratory

## **Subsurface Radar Investigations at the Pegasus Glacial-Ice Runway and Williams Field, McMurdo Station, Antarctica**

Steven A. Arcone, Allan J. Delaney and  
Wayne Tobiasson

November 1994

Accesion For	
NTIS	CRA&I
DTIC	TAB
Unannounced	
Justification _____	
By _____	
Distribution _____	
Avail Date _____	
Dist	Avail Loc / or Special
A-1	

*EX-10 QUALITY ASSURANCE*

Prepared for  
NATIONAL SCIENCE FOUNDATION  
and  
OFFICE OF THE CHIEF OF ENGINEERS

Approved for public release; distribution is unlimited.

## PREFACE

This report was prepared by Dr. Steven A. Arcone, Geophysicist, Allan J. Delaney, Physical Science Technician, both of the Snow and Ice Branch, Research Division, and Wayne Tobiasson, Civil Engineer, of the Civil and Geotechnical Engineering Research Branch, Experimental Engineering Division, U.S. Army Cold Regions Research and Engineering Laboratory. Funding for this research was provided by the National Science Foundation, Grant no. DPP-872 0063, and the Office of the Chief of Engineers through DA Project 4A161102AT24, *Research in Snow, Ice and Frozen Ground; Task SS, Properties of Cold Regions Materials; Work Unit E10, Electromagnetic Characteristics and Dynamics of Snow, Ice and Frozen Ground.*

This report was technically reviewed by Dr. Anthony Gow and George Blaisdell of CRREL.

The contents of this report are not to be used for advertising or promotional purposes. Citation of brand names does not constitute an official endorsement or approval of the use of such commercial products.

## CONTENTS

	Page
Preface .....	ii
Introduction .....	1
Radar equipment .....	1
General operation .....	1
Antennas .....	2
Waveforms and phase polarity .....	2
Antenna directivity .....	2
Field procedures and data processing .....	3
Field procedures .....	3
Data recording .....	4
Data processing .....	4
Site location .....	6
Results .....	6
Pegasus runway .....	6
Access road from Williams Field to Pegasus runway .....	10
Williams Field .....	14
Summary and conclusions .....	19
Literature cited .....	20
Appendix A: Airborne profile of a portion of the access road .....	23
Abstract .....	24

## ILLUSTRATIONS

### Figure

1. GPR 400-MHz wavelets reflected from a low density inclusion and brine within ice .....	2
2. Monostatic radar transmit–receive two-way directivity pattern for a finite size dipole operating over ice or snow of different dielectric permittivities and equivalent densities .....	3
3. 100-MHz antennas in tow behind a van .....	4
4. Wiggle trace display of a received scan and its equivalent line intensity display should the scan remain unchanged over a short distance.....	5
5. Approximate location of Williams Field and the Pegasus runway .....	5
6. Detail of the Pegasus runway site .....	6
7. Compressed profile at 400 MHz of the west side of the Pegasus runway .....	7
8. Uncompressed profiles at 400 MHz of two 500-ft (152-m) segments along the west side of Pegasus runway’s south end .....	8
9. Uncompressed profile at 400 MHz showing the density anomalies near the 10,500-ft (3200-m) distance.....	8
10. Computed density and $\epsilon$ profiles of a 5-m core, and a radar profile scan taken at the 10,492-ft (3198-m) distance along Pegasus runway .....	9
11. Uncompressed profile along Pegasus runway .....	9
12. Profile sections along the access road from the north end of Pegasus runway to Williams Field .....	10
13. Twenty-five-fold compressed, 100-MHz radar profile from the north end of Pegasus runway to point A .....	11
14. Deconvolved, 100-MHz profile of sections A–B and B–C .....	11
15. Expanded section of the profile in Figure 14 .....	12

Figure		Page
16. Compressed, deconvolved and migrated profile showing detail of the brine discontinuities and an exposure of a lower brine layer seen in section A-B in Figure 14 .....		12
17. 100-MHz deconvolved profile of sections C-D and D-WIL .....		13
18. Time and migrated profiles containing the brine discontinuities seen in sections C-D and D-WIL .....		13
19. Williams Field support facilities .....		14
20. Survey grid of the fuel spill site at Williams Field .....		14
21. Deconvolved, 400-MHz profiles of the fuel spill area .....		15
22. 400-MHz profile of the solid waste dump survey line .....		17
23. Plan view showing survey grid and location of the sewage sumps at Williams Field .....		17
24. Sewage area longitudinal 100-MHz profile and its migration using $\epsilon = 2.9$ ..		18
25. Migrated, 100-MHz cross-sectional profiles across the new and the old sewage sumps .....		19

## TABLES

### Table

1. Ice shelf thicknesses at locations shown in Figure 12 .....	10
--	----

# **Subsurface Radar Investigations at the Pegasus Glacial-Ice Runway and Williams Field, McMurdo Station, Antarctica**

STEVEN A. ARcone, ALLAN J. DELANEY AND WAYNE TOBIASSON

## **INTRODUCTION**

This report discusses the use of Ground-Penetrating Radar (GPR) to detect and map artificial and natural subsurface conditions at the Pegasus Glacial-Ice Runway (henceforth referred to as Pegasus runway), the access road to Pegasus runway and the Williams Field support facilities on the Ross Ice Shelf near McMurdo Station in Antarctica. GPR has been a common geophysical tool for near-surface geologic exploration in cold regions (e.g., Annan and Davis 1976, Kovacs and Morey 1979, Arcone and Delaney 1987, Delaney et al. 1991, Arcone et al. 1992, Arcone et al., in prep.<sup>1</sup>) owing to the excellent penetration of radio waves in ice and frozen soils and the vertical resolution of the short pulse. GPR, operating at a variety of bandwidths, can delineate subsurface features in snow and ice at depths ranging from less than 1 to over 100 m. Vertical resolution is determined by the bandwidth center frequency of the pulse used, and is generally about 20 cm in ice for antennas operating near 500 MHz, and less for materials with a higher dielectric constant such as permafrost. This exceptional resolution has also led to GPR becoming a popular device for utility detection and toxic and hazardous waste site characterization (e.g., Pilon 1992, Hanninen and Autio 1992) because subsurface debris, water and fuel spills, or the soil disturbances they cause, can present a strong radar target.

The objectives of these surveys were to characterize the ice and snow structure above the brine layer in the Pegasus-Williams Field area to support planned and ongoing operations projects, and to evaluate the ability of GPR to locate fuel spills, solid waste dumps and other conditions that might require remediation. GPR transducers operating at both 100- and 400-MHz pulse center frequencies

were towed by truck along lengthy profiles and by hand along short transects. Signal processing using deconvolution and migration was used to improve vertical resolution and spatial imaging. Limited coring, probing and excavation verified interpretation of GPR features of interest.

Radio echo sounding and GPR have been used extensively on the Ross Ice Shelf in the McMurdo Station vicinity (Clough 1973; Kovacs and Gow 1975, 1977a,b; Kovacs et al. 1982) and in other ice shelf locations far removed from McMurdo (e.g., Jezek 1980, Morey and Kovacs 1982). The most extensive studies near McMurdo were by Kovacs and Gow (1975) and Kovacs et al. (1982), who included drilling and ice core analysis with their radar profiles. Their work concentrated on characterizing the brine layer (an intrusive layer, probably of finite thickness, and fed mainly at the front of the ice shelf), reflections from which are the dominant feature in their records. Their data contain responses to many of the natural features such as cracking, folding and abrupt changes in brine level. Responses to these features are presented here also, but with the advantages of a higher resolution bandwidth. We also use digital recording for deconvolution processing to enhance resolution, and wave migration to transform distance-time records into distance-depth sections to give a more accurate spatial image.

## **RADAR EQUIPMENT**

### **General operation**

The radar used here comprises a Geophysical Survey Systems, Inc., SIR Model 4800 control unit, several different antennas, cables, a GSSI DT6000 digital tape recorder and a power supply. The control unit keys the transmitter on and off at 50 kHz

(synchronized with the receiver), and sets the scan rate (rate at which echo scans are compiled, generally 25.6 scans/s), scan time range and the Time Range Gain (TRG) to be applied to the scans. The transmitter antenna radiates a broadband wavelet that lasts from only a few to tens of nanoseconds (ns). A separate, identical receiver antenna is employed because echoes can return from near-surface events before the transmitter antenna has stopped radiating. The received signals are converted by sampling into an audio frequency facsimile for filtering, amplifying and recording.

### Antennas

All antennas are resistively loaded dipoles that radiate a wavelet lasting about 2 to 2.5 cycles. The 400-MHz antenna pair are flared dipoles with a tapered resistive loading, backshielded and housed in one unit (Model 3102, GSSI, Inc.) at a separation of about 15 cm. The 400-MHz transmitter is rated by the manufacturer at 8-W peak power excitation. The 100-MHz antenna pair (Model 3107, GSSI, Inc.) are of the same design, but each antenna is housed in a separate backshielded unit. The units were electrically shorted together, with the antenna centers separated by 1 m.

### Waveforms and phase polarity

A scan (Fig. 1) from a 400-MHz profile presented later shows events received from interfaces between

known dielectric contrasts. The scan shows a trigger pulse (labeled SOS for Start Of Scan), the Direct Coupling (DC) between transmitter and receiver antennas, and reflections from subsurface interfaces. The received wavelet forms in Figure 1 are close to the transmitted form and last only about two and one-half cycles. The instantaneous frequency, defined as the inverse of the time duration of one cycle, is about 375 MHz for the Model 3102 and close to 100 MHz for the Model 3107. For these studies where the signal levels were well above noise, the phase of an event is defined as the sequence of phase polarities for the first three half-cycles (labeled + or - in Fig. 1); other studies have used only the more visible, major half cycles (Arcone et al., in prep.<sup>1</sup>). The contrast in dielectric constant  $\epsilon$  across the reflecting interfaces determines whether the sequence is + + + or - - -. Reflections from interfaces of known dielectric contrasts, as well as the DC wavelet form, can be used as a phase reference (Arcone et al., in prep.<sup>1</sup>). A wavelet reflected from an interface containing a low-over-high  $\epsilon$  structure (e.g., ice over water) has the same + - + phase sequence as the DC and that from a high-over-low (e.g., ice over air) has a - + - sequence. Relative wavelet phase will be used to determine the nature of some of the reflectors within the ice and snow.

In view of the wavelet duration and the need for separation of top and bottom reflections, resolution of a thin air or water layer embedded in ice would require thicknesses of 75 and 8 cm respectively ( $\epsilon_{\text{air}} = 1$ ,  $\epsilon_{\text{water}} = 87$  at 0°C) for the 400-MHz antennas, and 300 and 32 cm at 100 MHz. Practically, far thinner layers can be resolved in a radar profile by observing phase continuity from scan to scan as the overlapping bottom reflection changes depth with distance. Resonance from layering can be characterized by the attachment of extra half-cycles to the primary layer reflection. The attachment of an extra half-cycle at 400 MHz would correspond to a 19-cm air layer and a 2-cm water layer. Many of the reflections seen later have no extra oscillations (i.e., resonance) as would occur in the response to an air layer of less than 10-cm thickness.

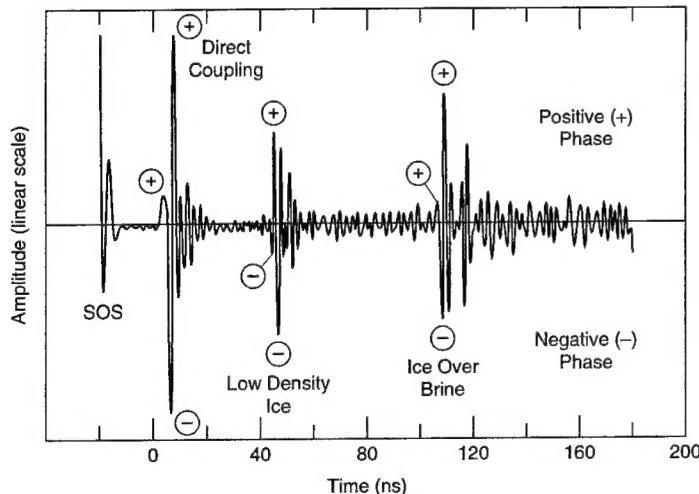
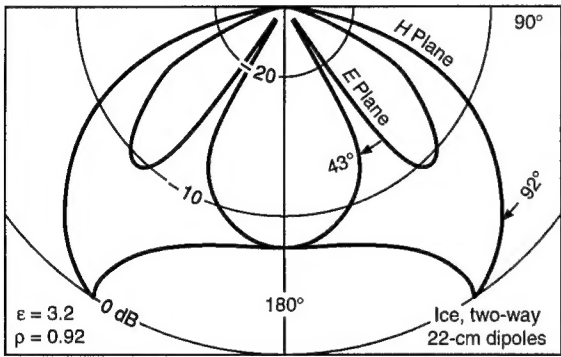
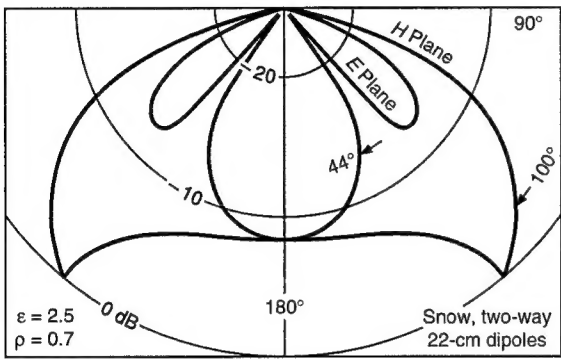
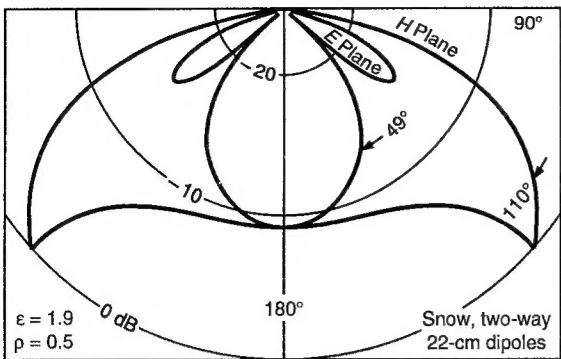


Figure 1. GPR 400-MHz wavelets reflected from a low density inclusion and brine within ice. Event SOS is an artificial start of scan signal; the ice surface is at 0 ns. 100-MHz wavelets have similar form. The sequences of half-cycle phase polarities (+ - + or - - -) indicate the dielectric contrast across the reflecting interface. The scan has been high-pass filtered.

### Antenna directivity

Theoretical transmitted radiation directivity for horizontal point dipoles on the surface of a dielectric half-space have been discussed by Annan (1973), Annan et al. (1975), Engheta et al. (1982) and Smith (1984). This



*Figure 2.* Monostatic radar transmit-receive two-way directivity pattern for a finite size dipole operating over ice or snow of different dielectric permittivities and equivalent densities  $\rho$ . The 3-dB angular width of the directivity in the E-plane, which is perpendicular to the direction of surveying, gives an approximate base for calculating the antenna width of sensitivity.

theory shows the directivity to be nonuniform, with nulls and lobes determined by the value of the critical angle  $\psi_c = \pm \sin^{-1}(1/n)$ , measured from vertical, where  $n = \sqrt{\epsilon}$  and  $\epsilon$  is the medium refractive index. Directivity nulls in the plane parallel to the antenna axis (electric field plane, or E-plane), and peak values in the plane perpendicular to the antenna axis

(magnetic field plane, or H-plane) occur at  $\psi_c$ , which for solid ice ( $n = 1.78$ ) is  $\pm 34^\circ$ .

The transmit-receive directivities for a horizontal, unshielded, finite-size radar antenna operating monostatically (i.e., two antennas with zero offset) on the surface of a homogeneous half-space with different values of  $\epsilon$  are shown in Figure 2. The E-plane is perpendicular to our profile directions and the H-plane is parallel. The directivities were computed for the far-field electric field strength by using the superposition of fields radiated by discrete antenna elements (Arcone 1994) and result from computing either the total energy content of the pulse (area under the waveform) or its peak value; both give nearly identical results. The patterns model the radiation response of the Model 3102, 400-MHz antennas to an idealized, 2.5-ns (400-MHz) half-cycle current pulse that progressively attenuates along each 11-cm half-length of the antenna; directivity patterns for the scaled, larger size 100-MHz antennas are nearly identical.

The patterns of Figure 2 are more directive than for a single transmitter antenna owing to multiplication of the identical transmit and receive directivities, and may be considered the radar response to an isotropic, polarization-insensitive, nondispersive point target. The two-way directivity in the E-plane shows a 3-dB beamwidth that progressively widens and sidelobes that progressively strengthen as  $\epsilon$  increases. The unorthodox H-plane pattern has maximum intensity in two scalloped lobes, and an effective beamwidth is not simply characterized. The single antenna gain in ice ( $\epsilon = 3.2$ ) is about 7 dB.

## FIELD PROCEDURES AND DATA PROCESSING

### Field procedures

We did the road and runway surveys by towing the antennas behind a van (Fig. 3). At the Williams Field support facilities, profiling was done by slowly dragging the antennas over the surface by hand along measured transects within a grid. All surveys were conducted with the antennas polarized perpendicular to the transect direction so that the more intense, but unorthodox, H-plane pattern was in the line of the transect. Event markers were placed artificially on the records at measured intervals, generally every 5 m for the shorter surveys at Williams Field. Scan durations were limited by the depth of the noise floor visible on the oscilloscope incorporated in the control unit, but were usually set to encompass the features of interest. We used 400 to



*Figure 3.* 100-MHz antennas in tow behind a van. No reflections from the van were apparent in the records. Van speed was generally about 2 m/s.

750 ns for the 100-MHz studies and 50 to 200 ns at 400 MHz. A round-trip propagation time of 100 ns corresponds to 8.4-m depth in solid (bubble-free) ice.

#### Data recording

All data were recorded at a scan rate of 25.6/second and scan sampling densities of 512 or 1024 8-bit words. Both an overall gain and a TRG were applied to all scans. The TRG is used to suppress the DC, amplify later returns and keep all signals within a level required for efficient digitization. The GSSI Model 4800 TRG function is fairly fixed in form and roughly compensates for the signal energy loss from spherical wavefront spreading. The TRG function does not significantly alter any waveforms in this study because their duration is always a small fraction of any scan.

#### Data processing

All data were compressed, or stacked, from five- to twenty-four-fold. Stacking suppresses random noise and marginally affected the spatial detail of the more intensive, shorter profiles, for which the stacked horizontal data density was about one scan per 10 cm. The lengths of the records between distance markers were equalized (i.e., "justified") to compensate for changes in towing speed. High-pass frequency filtering was used to alleviate scan-to-

scan gain variations resulting from inconsistent antenna-ground coupling. Low-pass filtering was used to alleviate high-frequency noise. Many profiles were further processed using predictive deconvolution to decrease the GPR wavelet length and thus increase resolution. This process does not generally retain the original phase structure of the wavelet. All filtering and migration (discussed below) used algorithms implemented by Boucher and Galinovsky (1990).

Echo time delay is generally transformed into depth on the basis of the simple echo delay formula for flat interfaces or point reflectors

$$d = ct/2n \quad (1)$$

where  $d$  = depth of a reflector (cm)

$t$  = echo time delay (ns)

$c$  = speed of electromagnetic waves in a vacuum (30 cm/ns).

The factor of two accounts for the round-trip propagation path. Many reflection profiles were migrated to transform the distance-time record of the raw data into the more meaningful distance-depth record because of irregular interface geometry and the presence of obscuring diffractions. The migrations used a single-layer Kirchhoff summation (e.g., Yilmaz 1987), an approach commonly used in glaci-

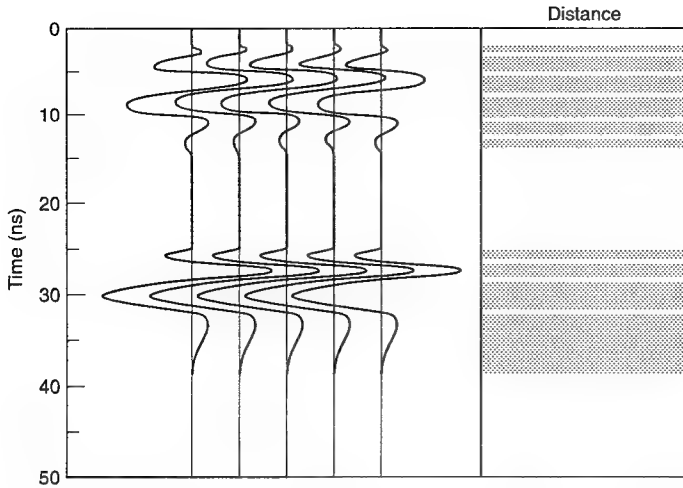


Figure 4. Wiggle trace display of a received scan and its equivalent line intensity display should the scan remain unchanged over a short distance.

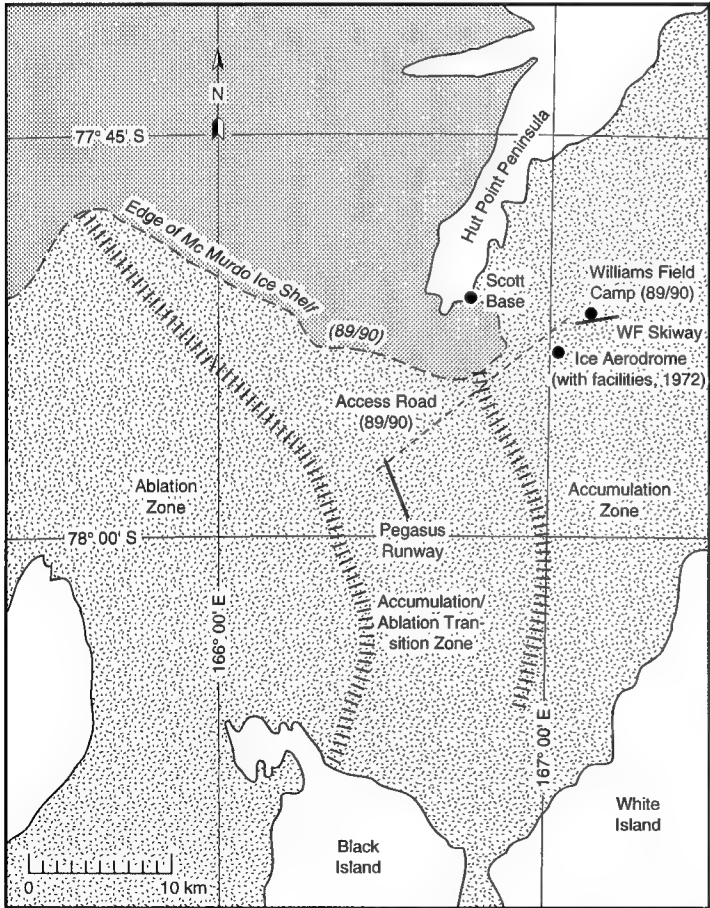


Figure 5. Approximate location of Williams Field and the Pegasus runway (adapted from Blaisdell et al. 1992 and Mellor 1993). Several sites were investigated at the airfield. Indicated boundaries for the ice shelf and transition zone are approximate also.

ology for single interface migration. Use of the single-layer approach is justified for subsurface conditions that are approximately homogeneous matrices of ice with local inclusions. The approach will not work if the inclusions are so dense that  $n$  is significantly elevated for a large portion of the ice. Features of the migration algorithm, the effect of the antenna directivity upon migration, and the use of migration for resolving subsurface glacial features are discussed by Arcone et al. (in prep.<sup>1</sup>)

Successful migration of a single interface depends on accurate knowledge of the velocity, or  $n$ , of the overlying layer. In the absence of drilling to obtain true reflector depth, single layer velocity can be determined at the surface either from surface refractions propagated between continuously separated antennas (Arcone 1984), from the asymptotic slopes of diffractions originating within or at the bottom of the layer, or by using a dual antenna arrangement to solve for both depth and  $n$  simultaneously (Kovacs et al. 1982). The first two methods were used here, but only the latter two give reasonably accurate results when  $n$  continually increases with depth, as is the case for snow, because surface refractions propagate mainly in the near-surface layers. Deep reflections and diffractions will spend a disproportionate amount of time within the upper layers because of the gradient of  $n$ , and so will give an effective  $n$  biased toward the surface. Migrations in these studies used a value  $n_m$  calculated from matching the slopes of the diffractions' asymptotes, generally to an accuracy of about  $\pm 2\%$ . This procedure produced good migrations of the diffractions, but  $n_m$  is not necessarily the average refractive index of the section migrated.

Data are displayed as echo-time-of-return vs. profile distance using either wiggle trace or line intensity format as depicted in Figure 4. A nonlinear scheme of scale intensity that emphasizes weaker events is used for the line intensity format. Profiles were printed on an Hewlett-Packard Paintjet printer. The quality of the printout was generally very good, but inferior to the display on the computer monitor.

## SITE LOCATION

All sites investigated were on the Ross Ice Shelf near McMurdo Station, Antarctica, and were associated with operations at Williams Field and the Pegasus runway (Fig. 5). Profiles were recorded along the Pegasus runway, the access road to the Pegasus runway, and three sites at the Williams Field support facilities. All sites were located in topographically depressed areas that were formed by maintenance activities that have removed snow, some continuously for several years. The surveys were performed between 14 and 18 January 1993. Weather during profiling was partially cloudy to overcast, with light winds and temperatures around 0°C. Surface melting is common on sunny days at the peak of the austral summer and small meltwater pools were encountered on the Pegasus runway and occasional wet snow at the Williams Field solid waste dump site.

Both the Pegasus runway (probably) and the Williams Field area are within the accumulation zone where snow is accumulating on top of glacial ice (Fig. 5). The Pegasus site, however, is in a transition zone of superimposed ice that is refrozen water from runoff and melted snow (Blaisdell et al. 1992), whereas Williams Field is in a zone of permanent snow. Cores taken by Blaisdell et al. along the Pegasus runway to 2.5-m depth reveal bubbly layers with densities as low as 0.6 g/cm<sup>3</sup>. Subsurface melt pools 1 to 1.5 m deep have been observed farther to the west within glacial "blue" ice and are attributable to the greenhouse effect (Paige 1968). The same process is known to form near-surface melt pools at Pegasus. They are generally prevented by roughening the surface. The accumulation zone has been well investigated, but particularly by Kovacs and Gow (1975) and Kovacs et al. (1982), who used radar and coring to study the infiltration of seawater into the snow; further discussion of their results is given later. We assume that snow exists at depth beneath the Pegasus site, based on the continuity of radar profiles of brine infiltration given below, but we do not have deep enough cores from this area to confirm this. Drilling in December 1991 by the Polar Ice Coring Office (PICO) revealed the ice shelf to be approximately 33 m thick at the north end of Pegasus runway. Freeboard above sea level was 4.8 m.

## RESULTS

### Pegasus runway

The objective of this survey was to determine if GPR could detect voids or water pockets near the

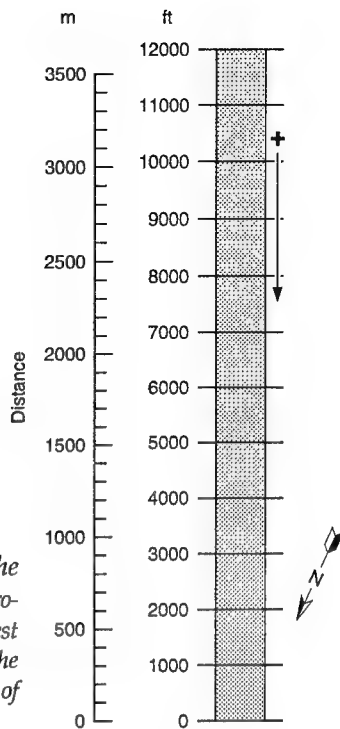


Figure 6. Detail of the Pegasus runway site. Profiles were run on the west side of the runway. The cross marks the location of a 5-m core.

surface, as these could cause failure of the ice pavement during wheeled landings of heavy cargo aircraft. Figure 6 depicts the runway and the placement of the profiles, all of which were run on the west side. The runway was flagged every 500 ft (152.4 m) over a distance of 10,500 ft (3200 m). The 100-MHz transducer unit was first used with a time range set to a depth of 58 m (for solid ice; greater for snow). The profile revealed only a few diffractions originating later than a strong horizon at about 9-m depth. Subsequently, 400-MHz profiles were run and only they are presented as they give much greater detail.

Figure 7 gives a compressed profile of the Pegasus runway from 11,000 to 0 ft (3353 to 0 m). At all depths and distances, the slopes of the diffraction asymptotes give an  $\varepsilon$  very near 3.2, the value for solid (bubble-free) ice, and which agrees with the ice core observations of Blaisdell et al. (1992) of predominantly solid ice in the upper 2 m. The dominant feature is the reflections originating between about 8- and 9-m depth. We believe that this radar horizon is brine infiltrating permeable snow at depth because it rises toward the north end (where the shelf thins) and continues into the accumulation zone (next section), where drilling has confirmed this interpretation (Kovacs et al. 1982). In the Pegasus area, the near-surface material is classified as superimposed ice, which is refrozen meltwater from snow and runoff. Alternatively, the horizon could be

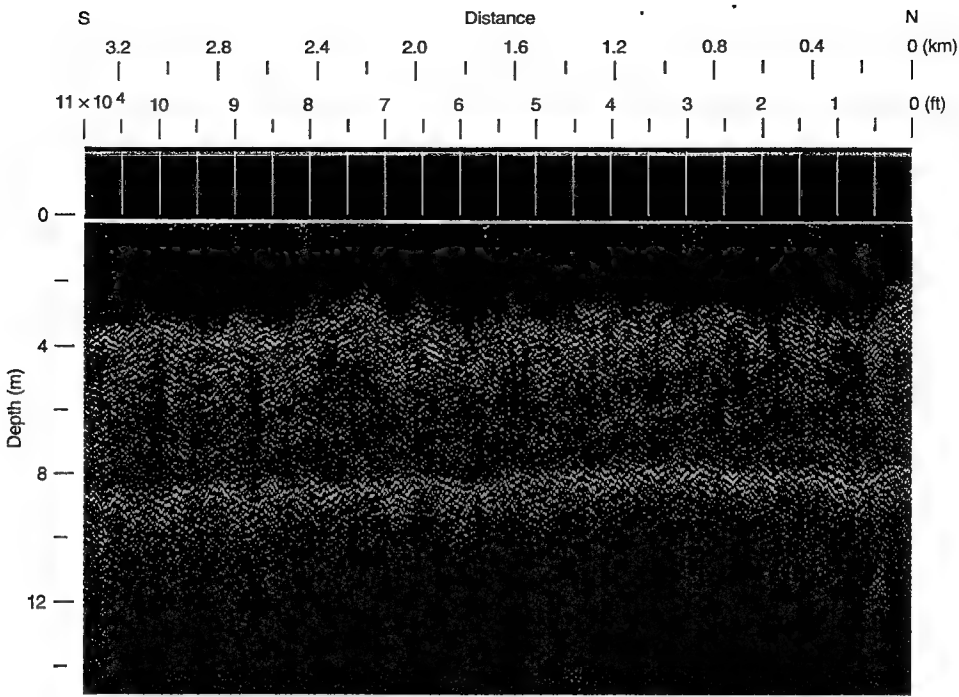


Figure 7. Compressed profile at 400 MHz of the west side of the Pegasus runway.

brine infiltration within permeable layers of the superimposed ice, or accreted sea ice,\* which, therefore, must be more than 20 m thick. A deep core would resolve this issue, but this was not the purpose of our survey.

Above the 8- to 9-m horizon in Figure 7 is a more diffuse level of reflections, with many horizons concentrated mainly between 3 and 5 m depth. These reflections are caused by density inhomogeneities in the ice, as discussed below. The time delay between the 3- to 5- and 8- to 9-m levels precludes interpretation of the 8- to 9-m reflections as multiples from the upper horizons. Reflections from the two levels are also distinctly different in structure, and in phase (discussed next).

More detailed, uncompressed profiles of runway sections are shown in Figure 8. These section profiles (as does the rest of the whole profile) reveal distinct linear horizons up to 30 m long between the 3- and 7-m depths. They are probably responses to bubble layers incorporated during melting and refreezing. Even greater resolution of the upper level events is seen in the 100-ns time range profile shown in Figure 9. At this range many events appear as single surface reflections, as would occur for dielectrically thin density anomalies. The brine "reflec-

tions" at 8–9 m in Figure 8 are actually composed of diffractions from discontinuities in the dielectric structure. These diffractions imply that the brine is intruding along discrete pathways.

As discussed earlier, reflection phase reversals relative to the direct coupling between these closely spaced transmit and receive antennas are ascribable to decreases in  $\epsilon$  with depth across a reflecting interface. Many of the upper level horizons in Figure 8 generally have a + - + structure (white-black-white banding in the profile—more apparent when the records are viewed edge on) to the strongest and most visible half-cycles of the wavelet, which indicates a negative dielectric anomaly (lower density). In contrast, the horizon at about the 9-m depth has a - + - wavelet structure (Fig. 1), which indicates a positive dielectric anomaly. This interpretation is verified by a 5-m ice core (Fig. 10) obtained at the 10,492-ft (3198-m) location on the runway where reflections occur in Figure 9 at about the 1.9- and 3.5-m depths. The core density anomalies are associated with air bubbles and occur at the depths of reflections in an individual scan from this station, also shown in Figure 10. Events 1 and 2 in the scan have phase sequences opposite that of the direct coupling. Event 3 has the same phase sequence and may be a secondary reflection from the bottom of the layer at 3.5 m. A secondary reflection from this lower layer would be visible because the layer is thicker than the layer at 1.9 m, as seen in the core

\* Personal communication with Dr. A.J. Gow, CRREL, 1994.

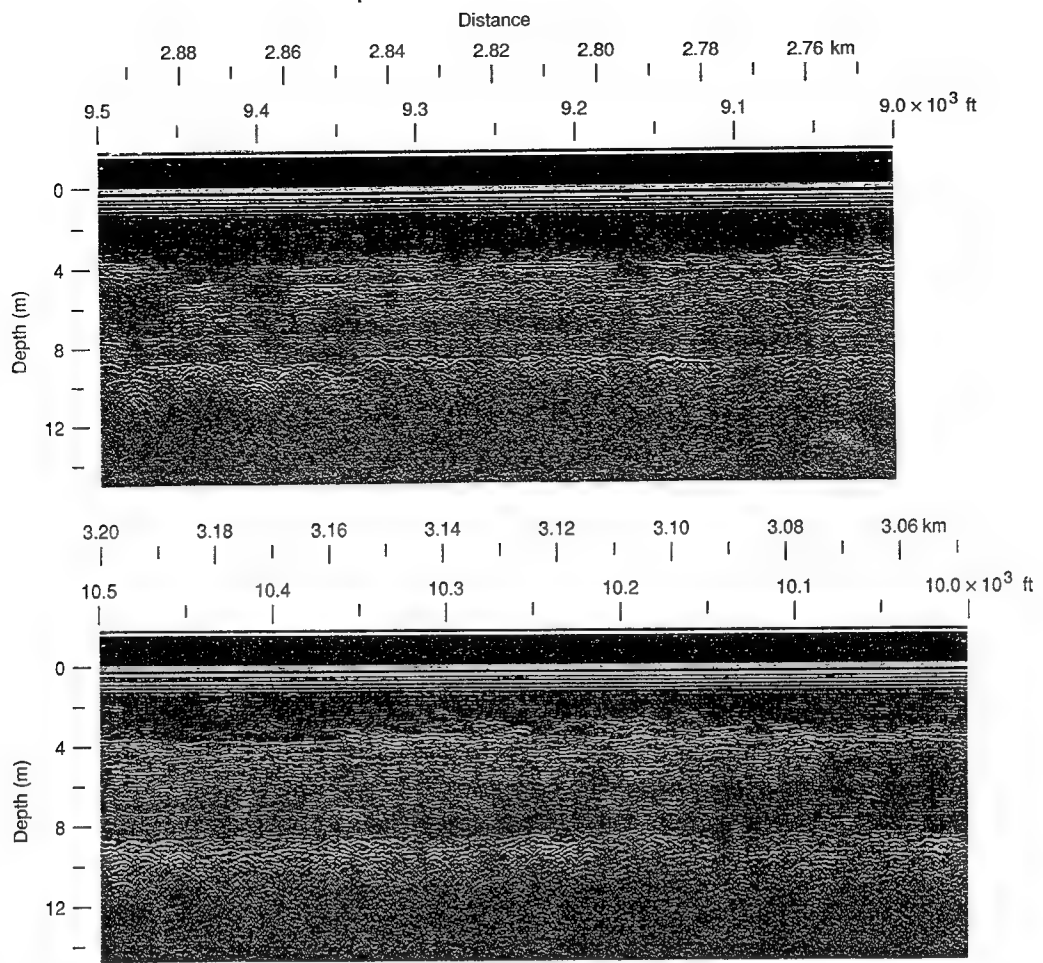


Figure 8. Uncompressed profiles at 400 MHz of two 500-ft (152-m) segments along the west side of Pegasus runway's south end. The horizons beginning at about 3 m depth appear to be bubble layers. The phase sequence of the major half-cycles of the wavelets is generally + - + (white-black-white banding) and is opposite to that of the brine reflections (- + -) at 9 m depth.

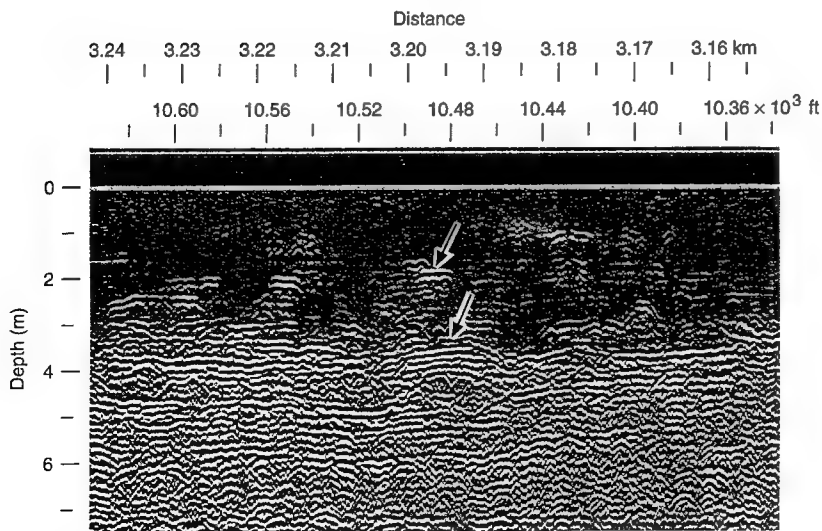
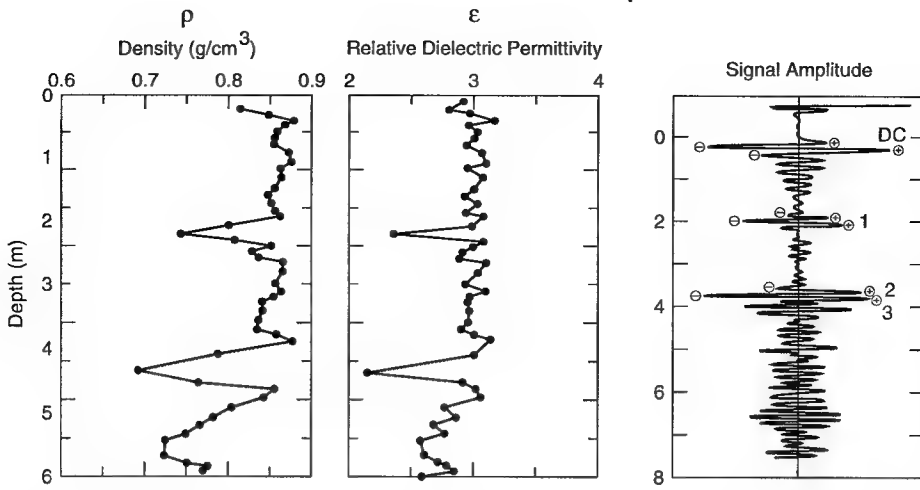
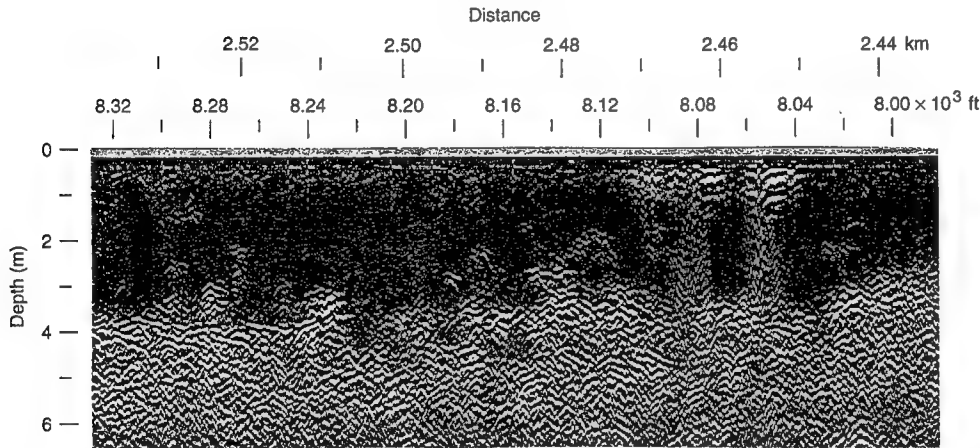


Figure 9. Uncompressed profile at 400 MHz showing the density anomalies near the 10,500-ft (3200-m) distance. Arrows point to the anomalies investigated in Figure 10. Some of the internal reflections persist to 30 m length.



*Figure 10. Computed density and  $\epsilon$  profiles of a 5-m core, and a radar profile scan taken at the 10,492-ft (3198-m) distance along Pegasus runway. Density is determined by weighing and measuring sample volume and is accurate to about 2%. Values of  $\epsilon$  based on the volumetric ratios of ice and air (e.g., Cumming 1952). Density is generally above 0.85, verifying the near-solid ice interpretation of  $\epsilon$  from the diffractions. The phase of the reflected wavelets relative to the direct coupling indicates a transition from high to low  $\epsilon$  at the reflecting interfaces (see Fig. 1 also).*



*Figure 11. Uncompressed profile along Pegasus runway. Near-surface melt pools occur between 8000 and 8100 ft (2438 and 2469 km). The record has been horizontally filtered to eliminate the surface coupling between antennas.*

profile. The separation of events 2 and 3 is 4 ns, which corresponds to a layer thickness of about 40 cm, given an  $\epsilon$  of 2.1, and is consistent with the anomaly width in the density profile.

Of particular concern to Pegasus operations are voids or melt pools within about 1 m of the surface. Several strong and extensive near-surface reflections were seen along the Pegasus profile between 8000 and 10,000 ft (2438 and 3048 m), some of which are shown in Figure 11. These are meltwater pools and they give a characteristic, diffraction-dominated response for localized, near-surface moisture. From 0

to 8000 ft (0 to 2438 m), there was near-surface meltwater along the profile at 158 locations, but each was limited to puddles less than about 20 cm in extent. Therefore, about 1% of the profile encountered near-surface or surface meltwater. An airborne or platform-mounted microwave survey would be better suited to this application, as all indications of meltwater appear to originate very near or at the surface. The existence of these small but weak areas in the ice of the runway is reason to continue to proof-test the ice pavement periodically with a load cart.

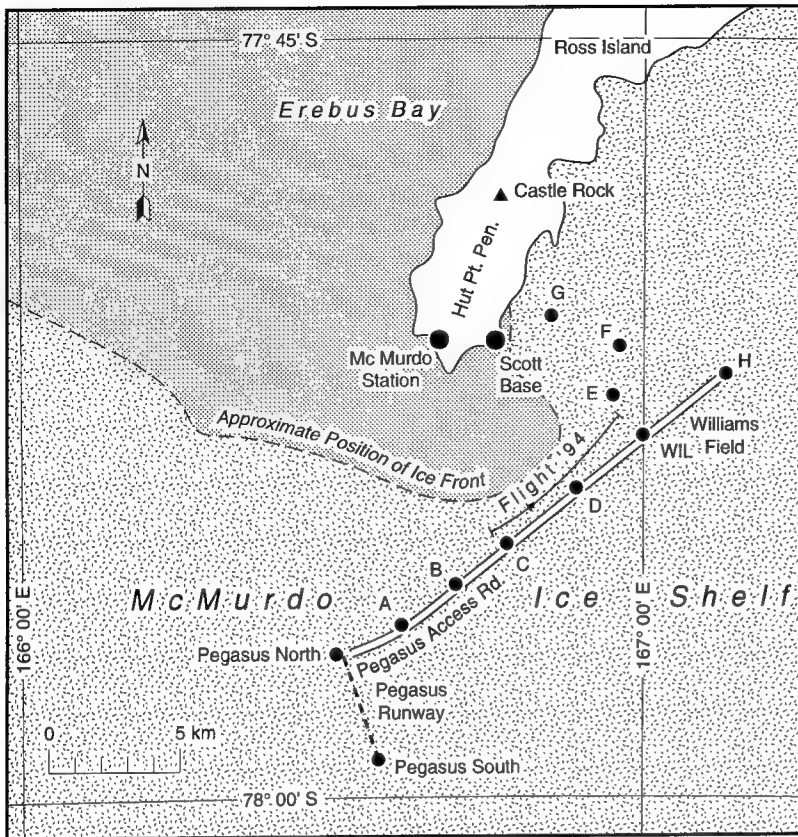


Figure 12. Profile sections (PEG—A—B—C—D—WIL) along the access road from Williams Field to the north end of Pegasus runway. Line marked Flight 94 is the approximate profile done by air in January 1994 and discussed in Appendix A.

#### Access road from Williams Field to Pegasus runway

The purpose of this survey was to profile the depth to the brine layer and to examine the access road for any unusual features, such as cracking in the ice. The approximate routing of the access road is shown in Figure 12. The road is divided into sections, the ends of which are indicated by letters. Recent hot water drilling (December 1991) by PICO has determined the ice shelf thicknesses presented in Table 1.

A compressed, 100-MHz profile for the access road section, progressing from the north end of the Pegasus runway to point A in Figure 12, is shown in Figure 13. The strong reflection seen at 8–9 m depth beneath the Pegasus runway continuously extends through this record and on to Williams Field, an area in which the horizon is known to be intruding seawater as discussed above. Only a vertical portion of the access road records is shown because there are no other primary reflections from beneath the brine layer, brine being highly absorbing of radio wave energy. We follow the terminology of Kovacs and

Table 1. Ice shelf thicknesses at locations shown in Figure 12.

Location	Thickness (m)
Pegasus North	33
A	40
B	36
C	26.5
D	31
H (Williams Field)	93

Gow (1975) in using the expression brine “layer,” as they point out that it cannot penetrate snow with a density greater than about 0.8. However, we can also call it a zone of brine permeation or penetration.

The 100-MHz antenna was used because the brine layer eventually deepens to the point where sample spacing within the radar scans would have been insufficient to reproduce the reflection waveforms accurately at 400 MHz. The accuracy of the distances shown for this and all other sections is estimated at about  $\pm 20$  m.

Although it is not apparent in the compressed profiles, the brine layer reflections themselves are not actually continuous reflections, but composites of multiple diffractions, as was seen at the Pegasus runway. These diffractions are scatter from discrete areas and show that the brine layer seems to intrude along discrete pathways within the snow. No diffractions originating at or above the brine layer that might be characteristic of cracking or crevassing are apparent in any of the access road profiles.

The depth scale at the start of Figure 13 is based on  $n_m=1.78$  ( $\epsilon=3.2$ ), which is determined by slopes of the diffraction asymptotes at the north end of the Pegasus runway where the profile starts. This solid ice value of  $\epsilon$  gives the minimum possible depth to the brine layer and is consistent with the density of ice cores taken near Pegasus (Blaisdell et al. 1992). The brine level depth varies from about 8 to nearly 10 m and stays at this level just beyond point C along the road, where it will be seen later that this level is being superseded by a younger and more shallow brine intrusion. Figure 13 also shows a different horizon dipping from southwest to northeast.

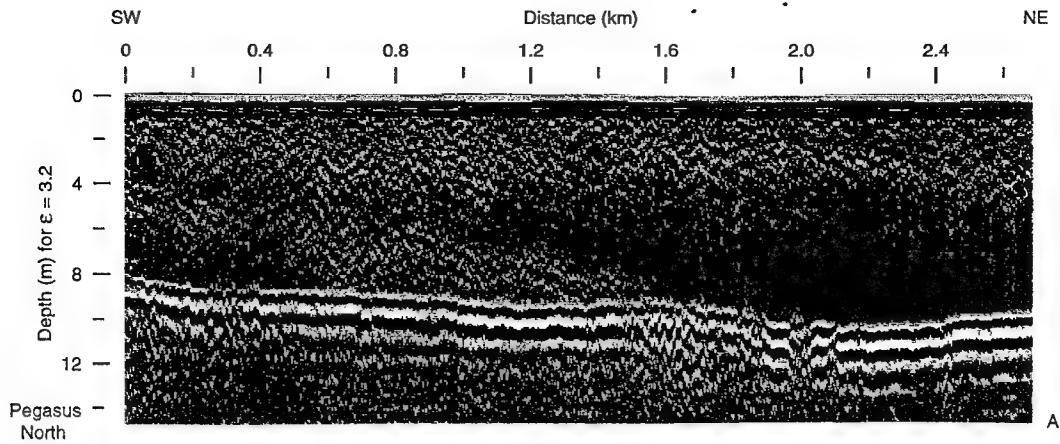


Figure 13. Twenty-five-fold compressed, 100-MHz radar profile from the north end of Pegasus runway to point A. Horizontal noise bands have been removed. The dominant feature is the returns from the brine layer. The origin of the diffuse horizon descending to the northeast in the first half of the profile is not known, but it cannot be the contact between snow and ice because there is no surface snow at Pegasus.

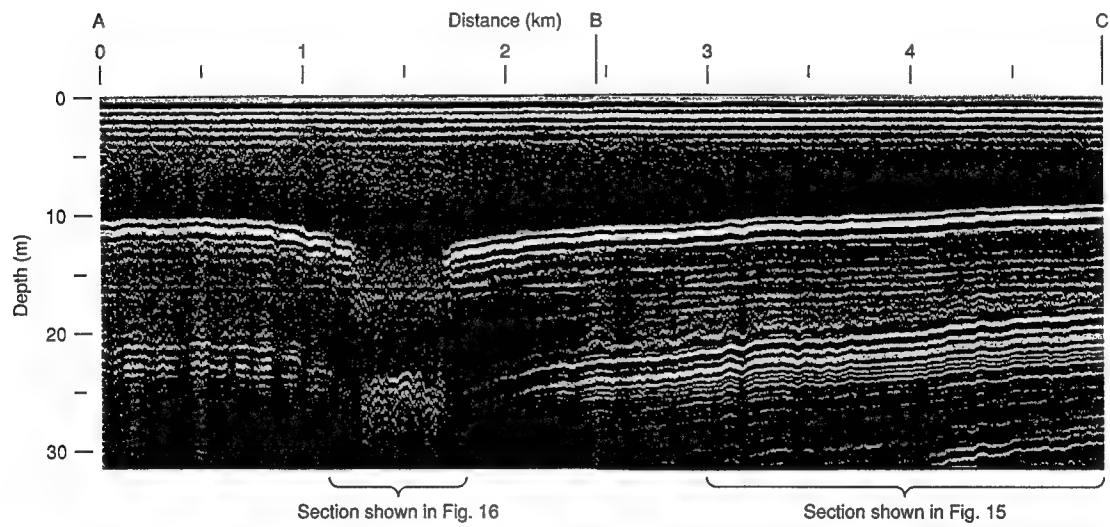


Figure 14. Deconvolved, 100-MHz profile of sections A-B and B-C.

The origin of this is not known, but it cannot be a snow-over-ice contact because there is no near-surface snow at Pegasus.

A deconvolved, 100-MHz profile for sections A-B and B-C of the road is shown in Figure 14. The profile contains two features of interest: folded stratification, and two apparent brine layers with discontinuities between A and B. The depth scale is based on diffraction slopes at point B that correspond to  $n_m=1.78$  ( $\epsilon = 3.2$ ), but there is evidence to show dielectric variability. Refraction profiles between A and B give a surface value  $n=1.4$ , which corresponds to a density of 0.5. At point B, the penetration rate of a hot point probe decreased (because of heat absorption by the brine) rapidly at 9.3 m; probing between the discontinuities is discussed be-

low. The radar profile gives a depth to brine of 10.0 m at point B. Using the hot point data for calibration suggests that  $n=1.9$ , which is slightly high. The discrepancy cannot be explained without knowing the exact gradient of the brine concentration, and the exact ray path through the dielectric stratification. The folding suggests that ray paths to the brine layer were not always direct, but the correction, discussed next, may be minor.

A deconvolved and expanded 100-MHz profile of the folding of density stratification in section B-C is shown in Figure 15. Scale compression and a horizontal (or "background removal") filter to remove the resonance of the direct coupling have been used to make the folding more visible. The stratification shows that the gradient of  $n$  is discontinuous; most

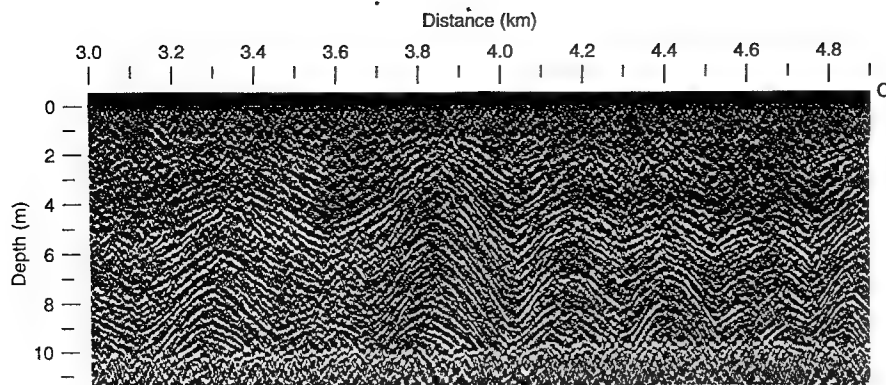


*Figure 15. Expanded section of the profile in Figure 14, showing detail of folding in section B-C. Background noise has been removed to show the diffractions that constitute the brine level discontinuity at 10 m depth.*

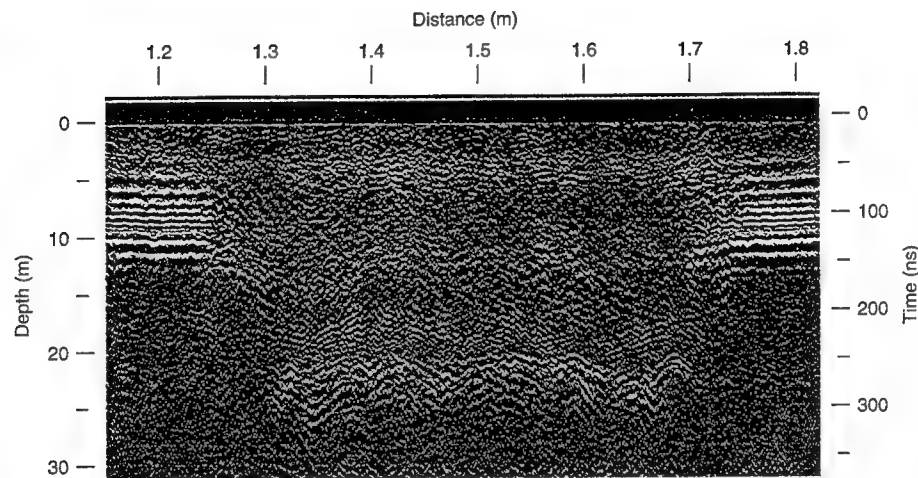


*Figure 16. Compressed, deconvolved and migrated profile showing detail of the brine discontinuities and an exposure of a lower brine layer seen in section A-B in Figure 14. The migration used  $\varepsilon = 3.2$ . The diffuse layer at about the 10-m depth probably contains brine.*

of the change must occur near the surface where  $n = 1.4$  because  $n_m$  is between 1.70 and 1.78. The width of one limb of a fold is about 150 m. This is five times the brine depth and corresponds to an angle of only about  $4^\circ$  from horizontal. This slope, along with the gradual change in  $n$  with depth, forces ray path bending to provide normal incidence at the brine layer and reflection back to the receiver antenna. The total bending is less than  $2^\circ$ , provides less than 1% correction to the ray path length and does not affect  $n_m$  significantly.

A deconvolved migration of the large discontinuity containing two diffuse radar horizons within section A-B is shown in more detail in Figure 16. Within the discontinuity, returns from the deeper horizon are stronger than those from higher in the snow so that these deeper events cannot be multiple reflections. The migration used an  $n_m$  of 1.78 based on the diffraction asymptotes, but slightly lesser values work nearly as well because precompression, needed to obtain an effective migration aperture,

mitigates migration noise. The profile reveals very little continuity in the upper horizon, but fairly good continuity in the lower. The penetration rate of a hot point probe half way between the ends of the discontinuity decreased rapidly at 9.6 m (the deeper layer was not reached), while the radar record shows this diffuse upper horizon to begin at about 9.8-m depth. Only the southwest side of the discontinuity shows any transition between upper and lower horizons, and both sides of the upper horizon have abrupt terminations. The upper horizon may represent a dense layer of snow into which brine from either side is slowly diffusing, while the lower horizon is either an exposed section of an older brine layer, sea water or accreted sea ice at the bottom of the shelf. Ice thicknesses measured a year earlier were 40 m at point A and 36 m at point B, which suggests that the lower horizon is not the bottom of the shelf.

Kovacs and Gow (1975) and Kovacs et al. (1982) give a thorough discussion of ice shelf breakout,

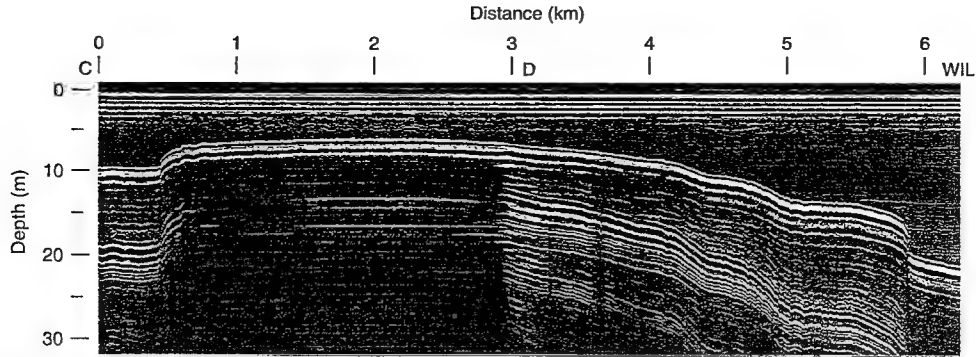


Figure 17. 100-MHz deconvolved profile of sections C-D and D-WIL. The depth scale is based on  $\epsilon = 2.7$ .

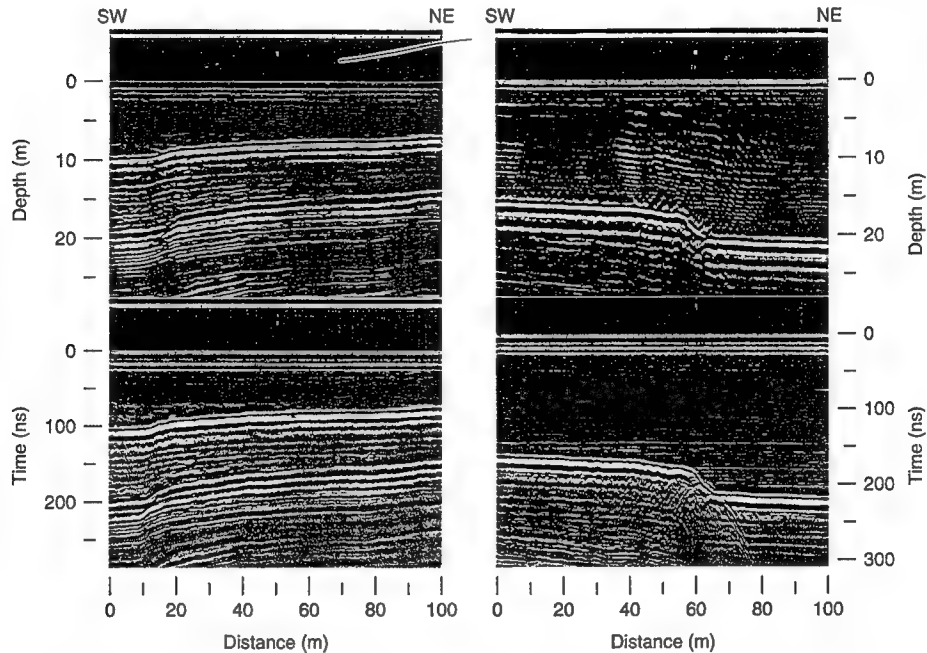


Figure 18. Time (bottom) and migrated profiles containing the brine discontinuities seen in sections C-D (left) and D-WIL (right). The expanded distance scale is 25× less than that of Figure 17. Diffractions indicate discontinuities. Apparent layering above the brine level in the migrated profile at right is an artifact of the migration.

subsequent brine “wave” intrusion and overriding of previous brine levels that existed before the breakout. Their radar data profile stepped intrusions as they extend away from the edge of the ice shelf. The example of Figure 16 seems to illustrate a cross section of this process at a location where the intruding front is not uniform. As mentioned above and as will be shown next, the 10-m brine level seen in Figure 16 is being overrun by a younger and more shallow brine level.

Profiles for sections C-D and D-WIL are shown in Figure 17. At Williams Field the ice shelf thickens because of snow accumulation and the brine level

drops below 20 m. Diffraction slopes at this end correspond to an  $n_m$  of 1.64 ( $\epsilon = 2.7$ ). Two brine level changes are seen here and these are the same type of features discussed above, but are more similar to the examples of Kovacs and Gow (1975). The brine layer rises just beyond point C because the edge of the ice shelf (where it contacts the sea) is closest between points C and D and then falls after point D as the sea ice contact becomes more distant (see Fig. 12). Both discontinuities are then part of the same brine front between points C and D. That brine front is the result of calving in this area. An airborne profile of this section, approximately from points C to WIL, was

run the following year and is shown in Appendix A.

Time and migrated sections of both brine discontinuities are shown in Figure 18. Only enough compression was used to permit the migration aperture of 61 scans (the maximum allowable by the software for a 1024 sampling density) to cover the diffractions adequately, but the scale is still 25 $\times$  less than that of Figure 17. In contrast to the discontinuities seen in Figure 16, the brine wave front between points C and D appears gradual, contains no significant diffractions (in the time section) and was probably traversed obliquely to the brine front normal. The front of the intrusion between D and WIL, however, contains at least two discontinuities as evidenced by the diffractions in the time section (Fig. 17). The migration shows that between the two breaks there is an almost continuous and coherent sloping reflection, which indicates a smooth brine front propagating northeast.

### Williams Field

A simplified map of Williams Field is shown in Figure 19. The layout shows the suspected location of a (presumed, surface) fuel spill near the fuel storage tanks, a suspected buried solid waste dump and old and new sewage sumps.

#### Fuel spill site

Our objectives at the spill site were to locate and delineate any fuel that may have not been removed from a previous Navy cleanup operation. During this cleanup, much snow was melted, which obviously refroze and has subsequently been buried. The main concern was that much of the fuel had percolated downward and was not retrieved.

A fuel spill in snow can provide a subtle dielectric contrast with the surrounding snow. Fuel has a typical dielectric constant  $\epsilon = 2.2$  and, when filling the pore spaces in snow of about 0.4 density, would produce an  $\epsilon$  of about 2.6. This would not provide much more contrast than would solid ice ( $\epsilon = 3.2$ ). If the uncontaminated snow already has an  $\epsilon = 2.8$  or higher, then it may not be permeable. This was obviously not the case because the fuel infiltrated the snowpack and was not ponded on the surface.

The layout of four profiles taken over the suspected fuel spill area is shown in Figure 20. The numbered boxes indicate the numbered fuel storage tanks. The diametric layout of the 65- to 80-m-long profiles was centered at the suspected origin of the

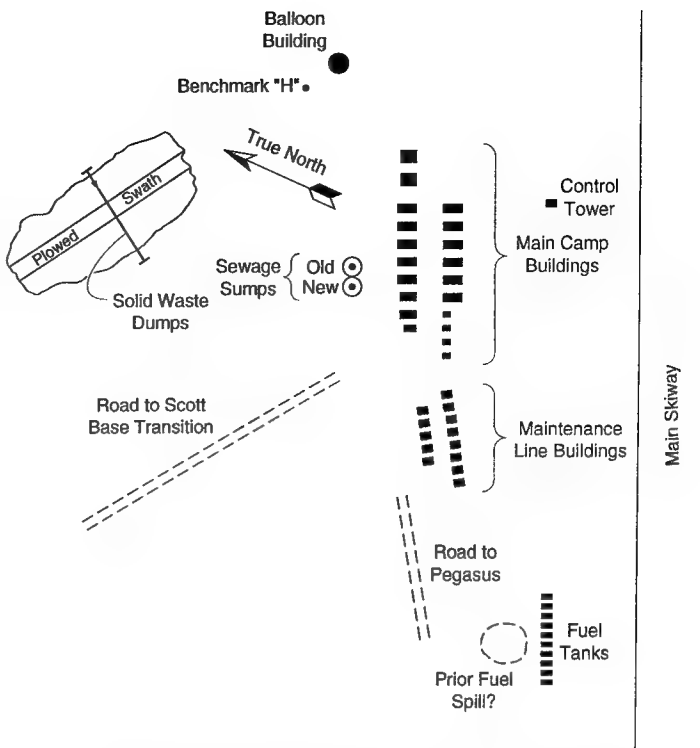


Figure 19. Williams Field support facilities (not to scale).

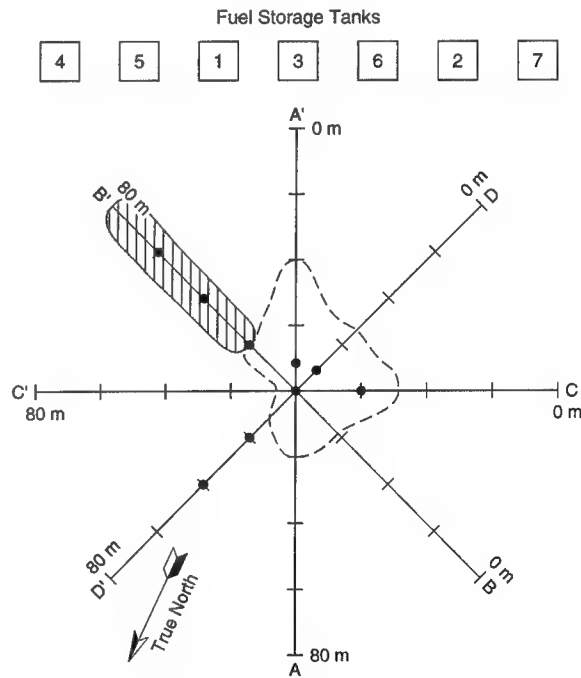


Figure 20. Survey grid of the fuel spill site at Williams Field; the position of the fuel tanks is for orientation only and not to scale. The dashed line indicates the suspected spill area interpreted from the radar profiles and the cross hatching indicates a dipping horizon that leads to a bright reflection at 7 m depth and 70 m distance along B-B'. The dots indicate particularly strong diffractions, which are at the 5- to 8-m depths.

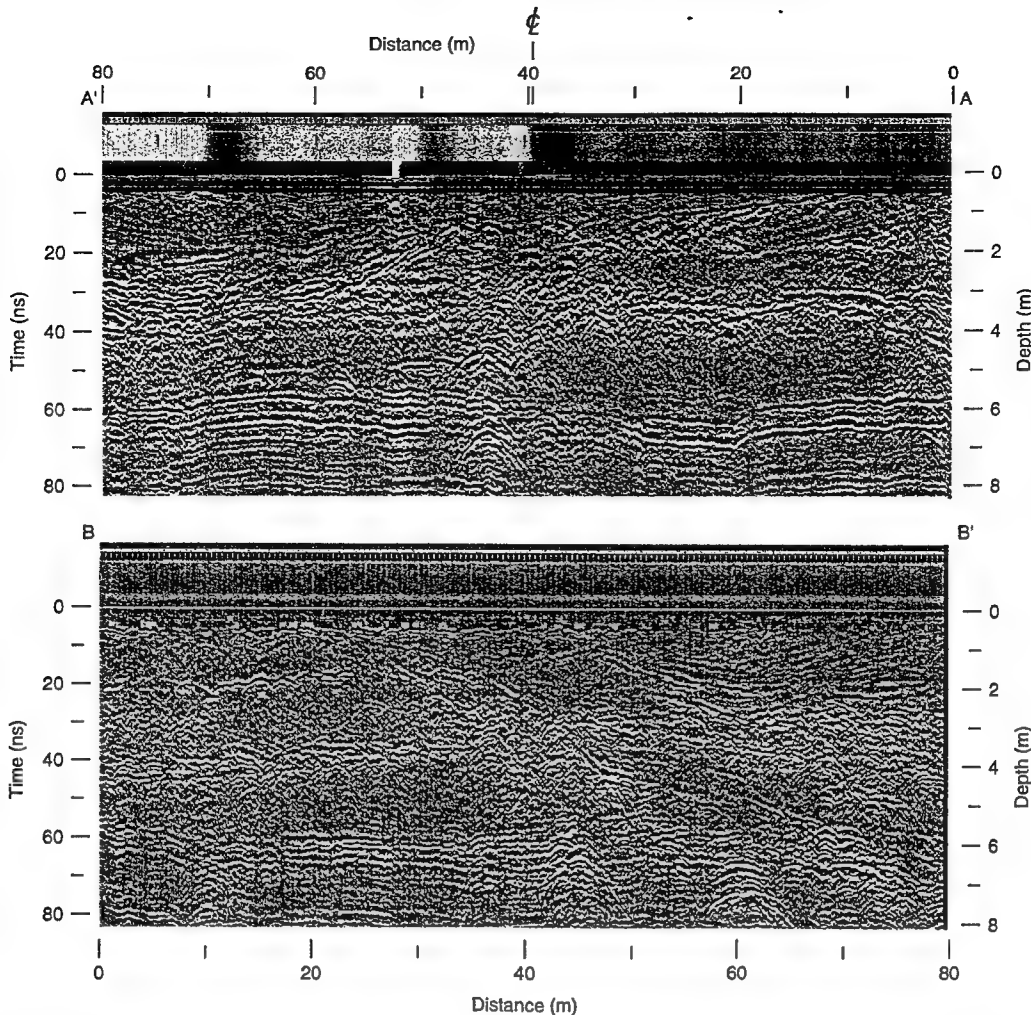


Figure 21. Deconvolved, 400-MHz profiles of the fuel spill area. The depth scale corresponds to an  $\epsilon = 2.3$ .

spill. Profiles were made with the 400-MHz transducer using a time range of 200 ns. However, within this time range, events that could possibly be a response to a fuel spill occurred within the first 80 ns throughout all profiles (Fig. 21). Each profile has been deconvolved and has had the antenna direct coupling removed to reveal any near-surface disturbance. Diffraction asymptotes show values of  $n_m = 1.52$  ( $\epsilon = 2.3$ ), which implies that any fuel spill was not pervasive and could be detected. This value of  $\epsilon$  gives a depth of about 8 m to the records, which should be deeper than any excavation done here. Migrations were not done because the diffractions highlight the disturbances.

All profiles in Figure 21 show linear horizons, presumed to be density layering in the snow. However, any of these horizons could be fuel or ice, but it is not known if fuel can concentrate rather than disperse in snow. There are particularly strong re-

flections at about 20, 40 and 60 ns, which translate to depths of about 2, 4 and 6 m respectively. All the profiles contain areas of strong diffractions concentrated in the central area, and some occur in multiples (e.g., at 44 m in A'-A and at 36 m in D-D'). In addition, Line B-B' shows a weak horizon that dips from 40- to 70-m distance, at which point it terminates in a particularly strong reflection. The area of the diffractions and the dipping horizon along B-B' may be the area of the fuel spill, the extent of which is delineated in Figure 20. By the time of this writing, drilling within the interpreted area of disturbance in Figure 20 had not been pursued.

#### Solid waste dump site

The objective of this limited survey was to verify the suspected area of a solid waste dump that was used for a number of years until 1990. Metal waste provides strong radar targets. The layout and ap-

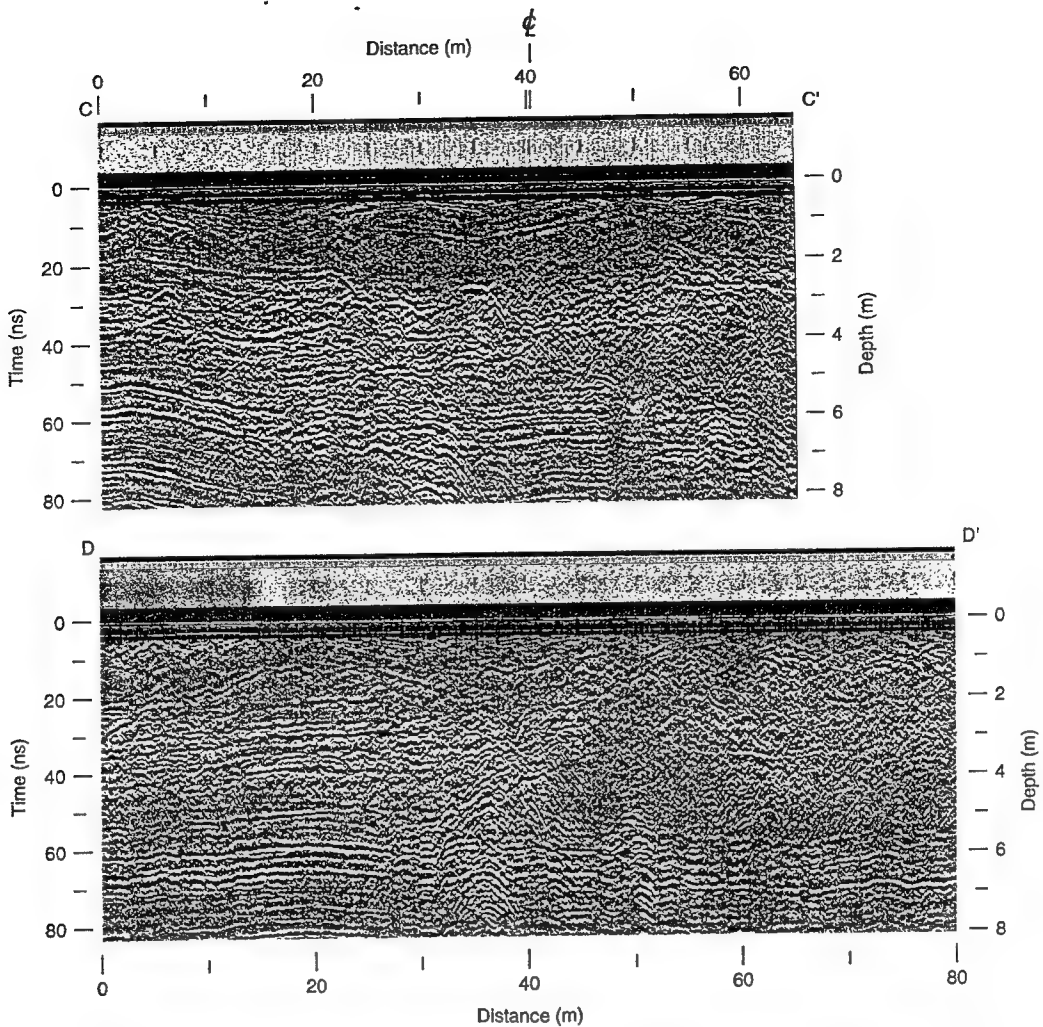


Figure 21 (cont'd). Deconvolved, 400-MHz profiles of the fuel spill area. The depth scale corresponds to an  $\epsilon = 2.3$ .

proximate location of a single, 100-m-long profile across the dump on the north side of Williams Field was shown in Figure 19. The profile was centered on and perpendicular to a plowed swath approximately 15 m wide. This swath was presumed to run through the suspected northwest-southeast orientation of the dump. The location of the line was not referenced exactly relative to any fixed landmarks, as this was only a test to see if GPR could find the buried waste, to be followed up with backhoe excavation to prove the value of the radar system to maintenance personnel at McMurdo Station.

The first 100 ns of the 400-MHz profile of the solid waste dump line is shown in Figure 22; no significant information was obtained at later return times. The upper part of the record shows subtle horizons that rise toward the center of the record. These horizons are assumed to be snow layers because they rise to where plowing had removed the

snow from the central part of the transect. Several anomalous returns appear beneath these horizons, with the strongest centered at the 20-, 55- and 87-m distances. All diffraction asymptotes associated with these disturbances give an  $n_m = 1.38$  ( $\epsilon = 1.9$ ), a value that corresponds with a snow density of approximately 0.5. This value of  $\epsilon$  is most likely a minimum for this material and shows the influence of the near-surface layers in refracting subsurface diffractions. The value is used to derive the depth scale of the profile, which provides a maximum range because the snow density increases with depth.

Subsequent to profiling, a section near the 55-m mark was excavated by bulldozer and metal debris was found at a depth of 3.4 m. This compares well with the bright reflection seen at about 3.7 m depth in Figure 22. Hard ice was encountered at the 1.5-m depth, and explains the earlier radar horizon at about 1.5 to 2 m depth near the 55-m mark.

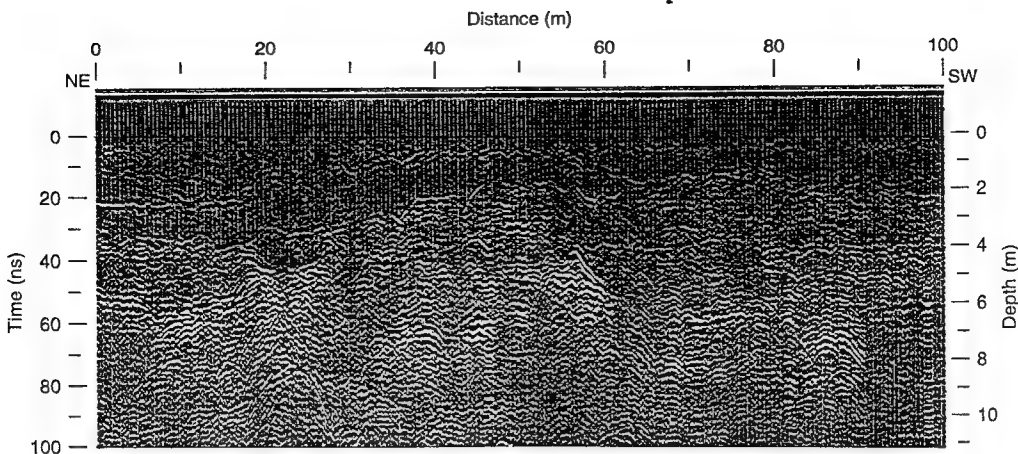


Figure 22. 400-MHz profile of the solid waste dump survey line. Upper horizons are presumably snow layers. The diffraction slopes give an  $\epsilon = 1.9$ , a value that gives a maximum depth range for the given time range. Excavation about the 55-m mark revealed hard ice at about the 1.5-m and metal debris at about the 3.4-m depths.

#### Sewage sumps

The objective of this last survey was to locate the upper surface of sewage-soaked snow at the buried sewage sumps (Fig. 19) and delineate its lateral extent. Snow soaked with liquid sewage provides a strong dielectric contrast with uncontaminated snow because the value of  $\epsilon$  for water at the freezing point is about 87, although it is slightly lower when filled with organic waste. The layout of one longitudinal and two cross-sectional profiles taken at the sewage sumps is shown in Figure 23. The sumps are

33 m apart in a west-southwest–east-northeast orientation. The eastern sump is older, filled with sewage and no longer in use. Some of the sewage there has probably refrozen. As more and more sewage is discharged into the snow, the contaminated zone rises. The western sump was put into use recently; thus, it is deeper. The dashed lines in Figure 23 give the extent of the sumps as extrapolated from the radar data.

A 100-MHz profile of the longitudinal line and its migration are shown in Figure 24. The profile was recorded at 500-ns time range in order to determine the depths to the sewage in the new sump and to the brine layer beneath it. The migration velocity corresponds to an  $n_m$  of 1.46 ( $\epsilon = 2.13$ ), but  $n_m$  values as large as 1.68 also produced diffractions that match some of the hyperbolas so that there is dielectric variability. Continuous plowing over many years has removed the lower density snow. The success of the migration is apparent from the linearity of the migrated features and the general absence of diffraction remnants. The conspicuous features in the migration are the upper surfaces of the brine layer at about 30 m depth, the upper surface of contaminated snow in the newer (deeper, less filled) sump at about 17 to 19 m depth, a (known) wooden box at the newer sump at about 5.5 m depth (sewer outfall head), and the sewage level in the older sump at about 8 to 10 m depth. The sewage in the newer sump appears to extend up to 45 m laterally from its discharge point (center line symbol), while sewage in the older sump

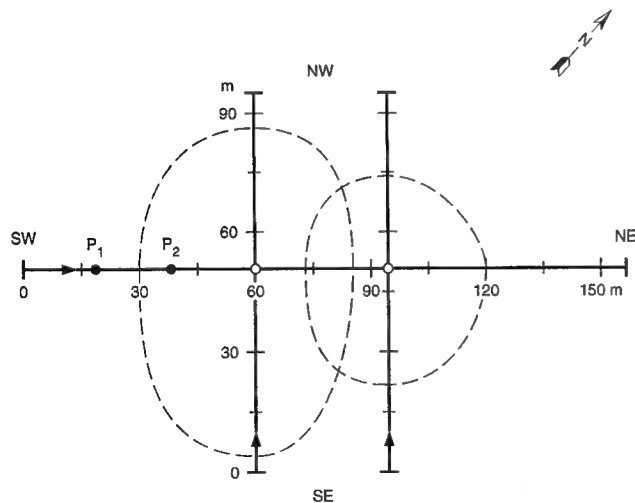


Figure 23. Plan view showing survey grid and location of the sewage sumps at Williams Field. The dashed lines indicate the zone of contaminated snow as interpreted from the radar data.  $P_1$  and  $P_2$  denote holes melted with a hot point drill to verify GPR findings.

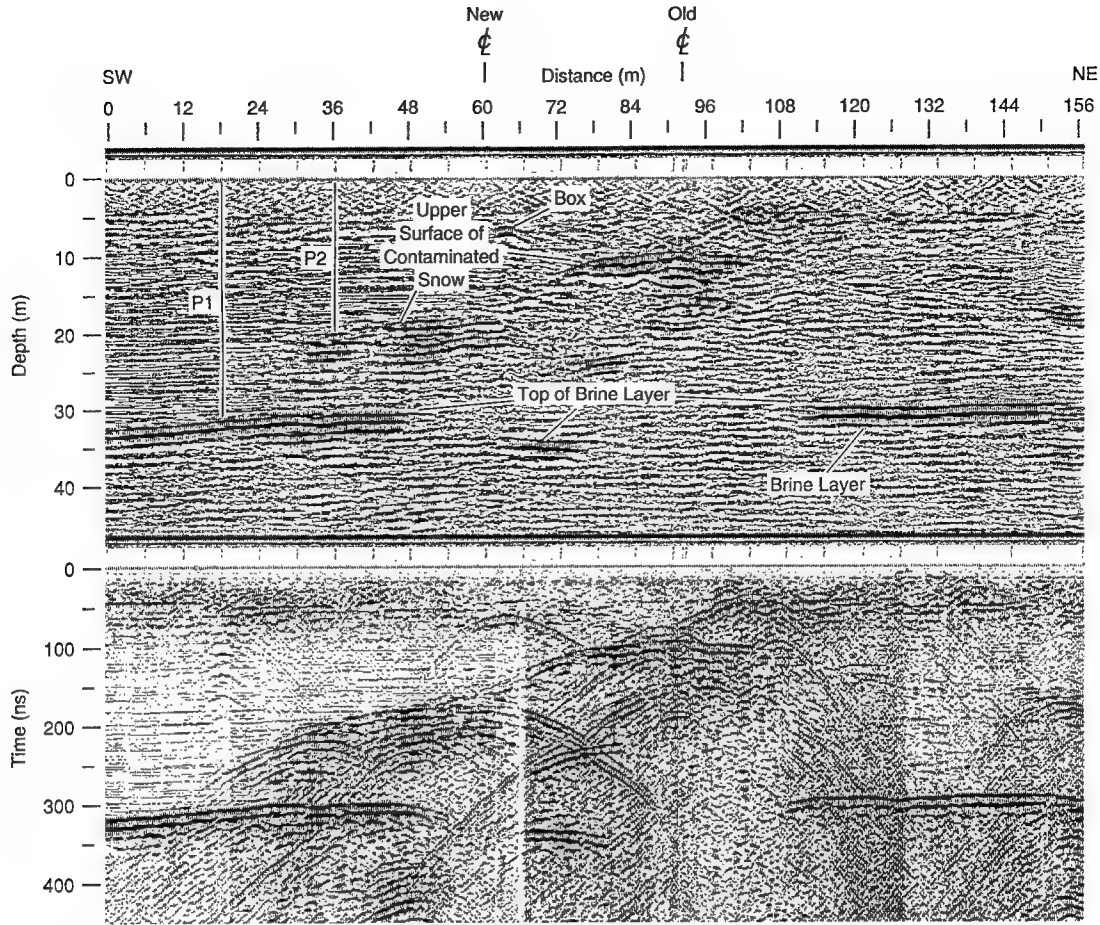


Figure 24. Sewage area longitudinal 100-MHz profile (bottom) and its migration using  $\epsilon = 2.8$ .

appears to extend laterally about 30 m. Taped distances at each discharge point gave surface-to-liquid depths of 16.8 and 7.2 m for the new and old sums respectively. Radar data very near those locations give depths of 17 and 7.8 m. The small discrepancy for the new sump is easily within the change of surface elevation near the new shaft because of frequent surface regrading in that area during the few weeks between when the distances were measured and the GPR survey was conducted.

A hot point drill was used to melt two holes where shown in Figures 23 and 24. When contaminated or brine-soaked snow is encountered, the rate of penetration of the heater slows considerably. Using this technique, we determined the depth to brine-soaked snow at point P<sub>1</sub> and sewage-soaked snow at point P<sub>2</sub> to be 30 and 18.8 m respectively. The GPR data determined these point depths to be 31 and 20 m, the discrepancy attributable to a less dense overburden than nearer the shaft.

Some of the reflecting horizons in Figure 24 appear to block penetration to the layers below, and we assume this to be the case for the interpreted sewage area in Figure 23. Most obvious is the blockage of radio wave energy penetration to the brine layer by the sewage. There is also apparent blockage of penetration to sewage in the newer sump by the older sewage between 72- and 90-m distance. Along this section, there appears to be an extra time delay to the new sump and this would be ascribable to the higher  $\epsilon$  of the sewage above. There is also a near-surface reflecting layer from 96 to 150 m, most likely related to a change in snow density, that may prohibit penetration to the east side of the older sump.

Figure 25 shows the migrated cross section profiles, each of which passed by a sewage outfall shaft. The cross section of the older sump shows it to extend more to the southeast. The cross section over the newer pit also shows extension to the south, where the level drops to almost 20 m depth.

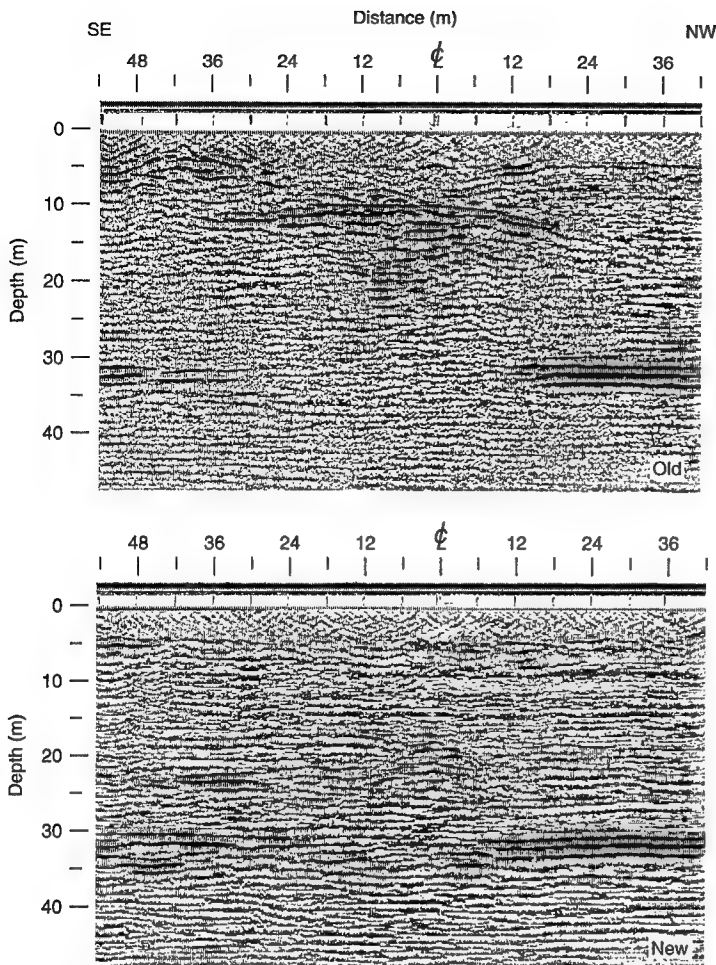


Figure 25. Migrated, 100-MHz cross-sectional profiles across the new and the old sewage sumps.

## SUMMARY AND CONCLUSIONS

Low density layers at the Pegasus runway, brine discontinuities along the Pegasus access road, metallic debris at the abandoned solid waste dump, and contaminated snow levels within sumps and their extent at Williams Field were clearly shown by reflections and diffractions. The contrast between the horizontal bubble layering at Pegasus and the folded density structure beneath parts of the access road is consistent with the ice and snow contrast between the two areas. No diffractions were seen along the access road that might indicate a major disturbance such as crevasses within the shelf structure. The radar results at the fuel spill site could not be confirmed because there has been no drilling or excavation to verify the findings.

Of particular interest is the extensive structure of low density layering seen beneath the Pegasus runway, generally throughout the 9-m depth to

the brine intrusion. Previously, only limited coring has revealed the presence of these bubble layers, but the radar profiles show how pervasive they are. Each of the profiles in Figures 8–10 are at successively greater resolution and reveal successively more detail, but the time and distance scales of Figure 9 seem best suited for revealing the overall structure of thin layers extending several tens of meters. A deep core and thin section analysis to at least 9 m depth would be helpful in determining the evolution of this structure and the nature of the ice or snow that allows brine to penetrate below the runway.

Diffractions from discontinuities in brine penetration within the ice shelf, as well as from the sewage deposits, responded well to the single-layer migration algorithm despite obvious variability in dielectric structure. The success of the migrations is judged by the absence of coherent artifacts (concave or convex hyperbolas) that characteristically occur when the migration velocity is too high, too low, or layering with significant velocity contrasts is present. This means that the refractive index values  $n_m$  used were effective averages for the overlying snow and ice.

The  $n_m$  values for the upper 10 m at the Williams Field sites range from 1.38 to 1.52. This range agrees with the average  $n$  of about 1.4 for the top 10 m or so of the ice shelf derived from the 1978 vertical density profiles in this area given by Kovacs et al. (1982). The  $n_m$  values for snow beneath the Pegasus access road are slightly higher. Only the upper meter or so of snow along this road has been compacted, so that a core analysis would be needed to verify if densities in this area are greater than along the line investigated by Kovacs et al.

The low loss of the snow and ice media should allow bandwidths centered as high as 1000 MHz to further improve vertical resolution. Such transducers are commercially available as are data densities of 2048 and 4096 samples/scan and 16-bit quantization to allow such bandwidths to acquire quality data at time ranges in excess of 200 ns. The Polar Operations Section, Division of Polar Programs, National Science Foundation, should consider purchasing a GPR system for use in Antarctica as these studies in the McMurdo area and others at the South Pole (Arcone et al., in prep.<sup>2</sup>) indicate that it could be used to answer many practical questions.

We also recommend that dielectric properties of mixtures of fuel and dense snow be measured as a function of temperature to determine if such properties differ significantly from those of dense snow alone. All forms of oil and fuel have very low dielectric constants and may not be readily detectable where they are dispersed in snow unless hydrocarbon properties change significantly with decreasing temperature. If concentration rather than dispersal occurs, then fuel and oil detection is routine because far more subtle dielectric contrasts are readily apparent, as was seen along the road from Pegasus runway to Williams Field.

## LITERATURE CITED

- Annan, A.P.** (1973) Radio interferometry depth sounding: Part I-Theoretical discussion. *Geophysics*, **38**(3): 557–580.
- Annan, A.P. and J. L. Davis** (1976) Impulse radar profiling in permafrost. *Radio Science*, **11** (4): 383–394.
- Annan, A.P., W.M. Waller, D.W. Strangway, J.R. Rossiter, J.D. Redman and R.D. Watts** (1975) The electromagnetic response of a low-loss, 2-layer, dielectric earth for horizontal electric dipole excitation. *Geophysics*, **40**(2): 285–298.
- Arcone, S.A.** (1984) Field observations of electromagnetic pulse propagation in dielectric slabs. *Geophysics*, **49**(10): 1763–1773.
- Arcone, S.A.** (in press) Numerical studies of the radiation patterns of resistively-loaded dipoles. *Journal of Applied Geophysics*.
- Arcone, S.A. and A.J. Delaney** (1987) Helicopter-borne short-pulse radar profiles of river-ice sheets in Alaska. *Journal of Glaciology*, **97**(1): 333–341.
- Arcone, S.A., E.F. Chacho, Jr. and A.J. Delaney** (1992) Short-pulse radar detection of groundwater in the Sagavanirktok River flood plain in early Spring. *Water Resources Research*, **28**(11): 2925–2936.
- Arcone, S.A., D.E. Lawson and A.J. Delaney** (in prep.<sup>1</sup>) Short-pulse radar wavelet recovery and resolution of dielectric contrasts in englacial and basal ice at Matanuska Glacier, Alaska. *Journal of Glaciology*.
- Arcone, S.A., A.J. Delaney and W. Tobiasson** (in prep.<sup>2</sup>) Ground-penetrating radar investigations of the proposed Dome-CARA tunnel route and utilities at South Pole Station, Antarctica. USA Cold Regions Research and Engineering Laboratory, CRREL report.
- Blaisdell, G.L., V. Klokov and D. Diemand** (1992) Development of a wheeled runway for McMurdo on the Ross Ice Shelf. USA Cold Regions Research and Engineering Laboratory, CRREL contract report.
- Boucher, R. and L. Galinovsky** (1990) RADAN 3.0 (signal processing software). N. Salem, New Hampshire: Geophysical Survey Systems, Inc.
- Clough, J.W.** (1973) Radio echo-sounding: brine percolation layer. *Journal of Glaciology*, **12**(64): 141–143.
- Cumming, W.A.** (1952) The dielectric properties of ice and snow at 3.2 centimeters. *Journal of Applied Physics*, **23**(7): 768–773.
- Delaney, A.J. and S.A. Arcone** (1994) Detection of crevasses near McMurdo Station, Antarctica, with airborne short-pulse radar. In *Proceedings: XXIII SCALOP Symposium, 29 August–9 September, Rome, Italy*.
- Delaney, A.J., S.A. Arcone and E.F. Chacho, Jr.** (1991) Winter short-pulse radar studies on the Tanana River, Alaska. *Arctic*, **43**: 244–250.
- Engheta, N., C.H. Pappas and C. Elachi** (1982) Radiation patterns of interfacial dipole antennas. *Radio Science*, **17**(6): 1557–1566.
- Hanninen, P. and S. Autio (Ed.)** (1992) *Proceedings, IV International Conference on Ground Penetrating Radar, 8–13 June 1992, Rovaniemi, Finland*. Espoo, Finland: Geological Survey of Finland, Special Paper 16.
- Jezek, K.C.** (1980) Radar investigations of the Ross Ice Shelf. Ph.D. dissertation. Madison: University of Wisconsin (unpublished).
- Kovacs, A. and A.J. Gow** (1975) Brine infiltration in the McMurdo Ice Shelf, McMurdo Sound, Antarctica. *Journal of Geophysical Research*, **80**(15): 1957–1961.
- Kovacs, A. and A.J. Gow** (1977a) Dielectric constant and reflection coefficient of the snow surface and near-surface internal layers in the McMurdo Ice Shelf. *Antarctic Journal of the United States*, **12**(4): 137–138.
- Kovacs, A. and A.J. Gow** (1977b) Subsurface measurements of the Ross Ice Shelf, McMurdo Sound, Antarctica. *Antarctic Journal of the United States*, **12**(4): 146–148.
- Kovacs, A. and R.M. Morey** (1979) Remote detection of massive ice in permafrost along the Alyeska Pipeline and the pump station feeder gas pipeline. In *Proceedings of the Specialty Conference on Pipelines in Adverse Environments, ASCE, New Orleans, Louisiana*, p. 268–279.
- Kovacs, A., A.J. Gow, J.H. Cragin and R.M. Morey** (1982) The brine zone in the McMurdo Ice Shelf, Antarctica. USA Cold Regions Research and Engineering Laboratory, CRREL Report 82-39.

- Mellor, M.** (1993) Notes on Antarctic aviation. USA Cold Regions Research and Engineering Laboratory, CRREL Report 93-14.
- Morey, R.M. and A. Kovacs** (1982) The effects of conductivity on high-resolution impulse radar sounding, Ross Ice Shelf, Antarctica. USA Cold Regions Research and Engineering Laboratory, CRREL Report 82-42.
- Paige, R.A.** (1968) Sub-surface melt pools in the McMurdo Ice Shelf, Antarctica. *Journal of Glaciology*, 7(51): 511–516.
- Pilon, J. (Ed.)** (1992) *Proceedings, II International Conference on Ground Penetrating Radar, 26–28 May 1988, Ottawa, Canada*. Ottawa: Canadian Research Council, Department of Energy, Mines and Resources, Geological Survey of Canada Paper 90-4.
- Smith, G.S.** (1984) Directive properties of antennas for transmission into a material half-space. *IEEE Transactions on Antennas and Propagation*, AP-32: 232–246.
- Yilmaz, O.** (1987) *Seismic Data Processing*. Tulsa, Oklahoma: Society of Exploration Geophysicists.

## APPENDIX A: AIRBORNE PROFILE OF A PORTION OF THE ACCESS ROAD

During January 1994, extensive surveying was done in the McMurdo area to demonstrate crevasse detection by airborne radar (Delaney and Arcone 1994). One of the flights was almost directly over section C-WIL along the access road from the Pegasus runway to Williams Field (Fig. 12) and the radar profile is shown in Figure A1. The center frequency of the wavelet is approximately 200 MHz. The profile has been corrected for flight altitude variations, deconvolved and horizontally filtered to remove aircraft reflections.

The airborne profile shows the main features seen in Figure 17, including the rising brine level between points C and D and at least one of the discontinuities. Although the airborne profile is apparently closer to the sea ice and does not extend as far northeast as does the surface profile, the deepening brine level beyond the discontinuity near point WIL seems to be deeper and extend further than when seen from the surface. This is attributable to inaccurate coordinate control, movement of the ice shelf during the year and, probably, complicated brine intrusion and ice shelf dynamics.

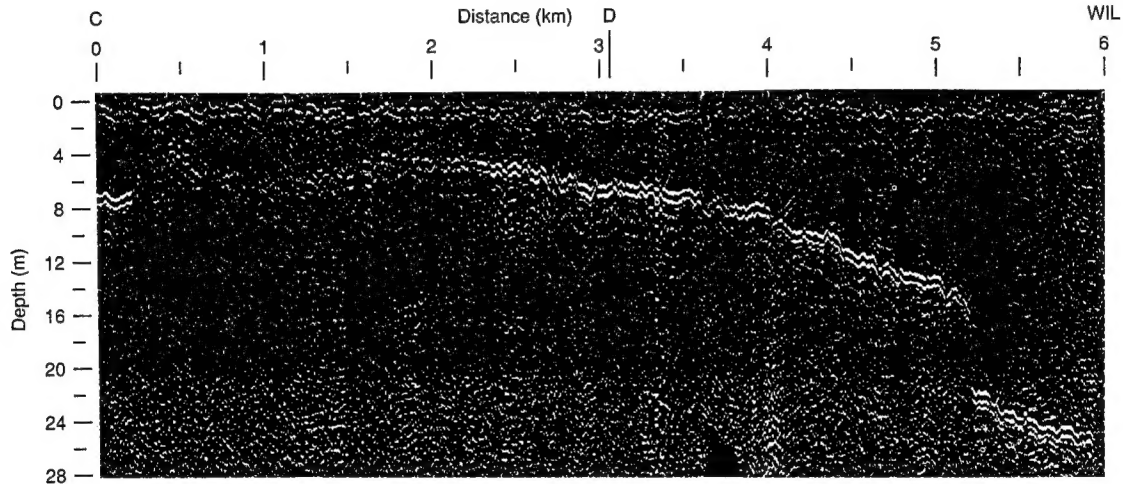


*Figure A1. Airborne radar profile at 200 MHz near the Pegasus runway access road approximately between points C and WIL (Fig. 12). The depth scale is based on  $\epsilon = 2.7$ . The profile is to be compared with that in Figure 17. The profile has been corrected for aircraft altitude fluctuations and has been deconvolved. The weak response of the brine layer in the southwest half may be attributable to a rough surface.*

# REPORT DOCUMENTATION PAGE

*Form Approved  
OMB No. 0704-0188*

Public reporting burden for this collection of information is estimated to average 1 hour per response, including the time for reviewing instructions, searching existing data sources, gathering and maintaining the data needed, and completing and reviewing the collection of information. Send comments regarding this burden estimate or any other aspect of this collection of information, including suggestion for reducing this burden, to Washington Headquarters Services, Directorate for Information Operations and Reports, 1215 Jefferson Davis Highway, Suite 1204, Arlington, VA 22202-4302, and to the Office of Management and Budget, Paperwork Reduction Project (0704-0188), Washington, DC 20503.

1. AGENCY USE ONLY (Leave blank)	2. REPORT DATE November 1994	3. REPORT TYPE AND DATES COVERED	
4. TITLE AND SUBTITLE  Subsurface Radar Investigations at the Pegasus Glacial-Ice Runway and Williams Field, McMurdo Station, Antarctica		5. FUNDING NUMBERS	
6. AUTHORS  Steven A. Arcone, Allan J. Delaney and Wayne Tobiasson			
7. PERFORMING ORGANIZATION NAME(S) AND ADDRESS(ES)  U.S. Army Cold Regions Research and Engineering Laboratory 72 Lyme Road Hanover, New Hampshire 03755-1290		8. PERFORMING ORGANIZATION REPORT NUMBER  CRREL Report 94-12	
9. SPONSORING/MONITORING AGENCY NAME(S) AND ADDRESS(ES)  National Science Foundation Washington, D.C.  Office of the Chief of Engineers Washington, D.C. 20314-1000		10. SPONSORING/MONITORING AGENCY REPORT NUMBER	
11. SUPPLEMENTARY NOTES			
12a. DISTRIBUTION/AVAILABILITY STATEMENT  Approved for public release; distribution is unlimited.  Available from NTIS, Springfield, Virginia 22161		12b. DISTRIBUTION CODE	
13. ABSTRACT (Maximum 200 words)  Subsurface radar was used to profile ice and snow conditions on the Ross Ice Shelf at McMurdo Station, Antarctica, during mid-January 1993. Deconvolution and migration were often used to improve vertical resolution and spatial imaging. Profiles at a pulse center frequency of 400 MHz along the 3.2-km-long Pegasus ice runway show many low-density horizons above 9 m depth that are up to 30 m long. They are associated with air bubbles included during refreezing of meltwater and are interpreted as layers between a few and tens of centimeters thick. There is a strong reflecting horizon at about 9 m depth that is probably from brine intrusion as it is continuous with the intrusion into the snow to the east. Diffraction asymptotes give a dielectric constant near 3.2 for material above the brine level, a value that implies near-solid ice. Profiles at 100 MHz along the road between Pegasus runway and Williams Field in the accumulation zone show snow features such as layer deformation and intrusive brine layers that both abruptly and gradually change in depth. A single profile at a relic solid waste dump at Williams Field detected buried debris and ice within the upper 7 m. A survey of a suspected fuel spill shows some local disturbances near the center, but no excavation was done to verify the findings. Profiles traversing the sewage sumps at Williams Field outline the extent of the sewage deposition, and give depths to contaminated snow that closely agree with observation. Despite variability in dielectric properties, single-layer migration effectively improves the resolution of subsurface conditions. Recommendations are made for future surveys.			
14. SUBJECT TERMS  Antarctica Cold regions		15. NUMBER OF PAGES 29	
Ground penetrating radar McMurdo Station		16. PRICE CODE	
17. SECURITY CLASSIFICATION OF REPORT UNCLASSIFIED	18. SECURITY CLASSIFICATION OF THIS PAGE UNCLASSIFIED	19. SECURITY CLASSIFICATION OF ABSTRACT UNCLASSIFIED	20. LIMITATION OF ABSTRACT UL